CHALMERS
UNIVERSITY OF TECHNOLOGY

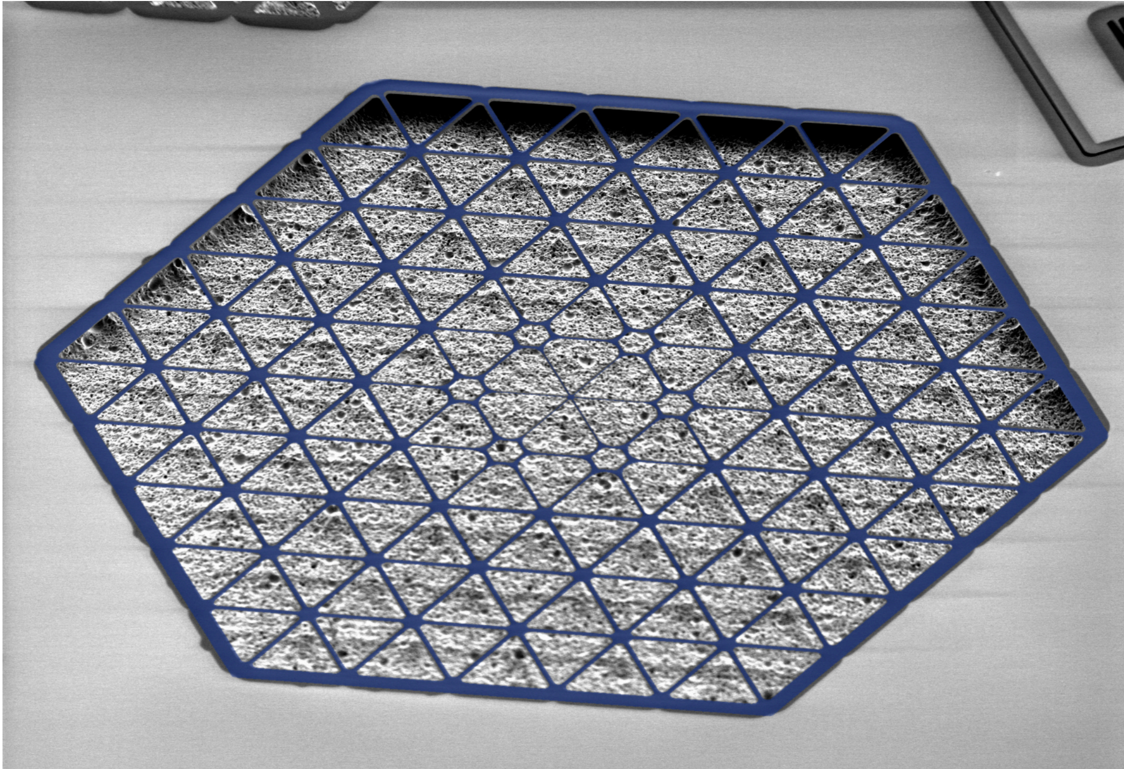

Tensile-strained crystalline aluminium nitride nanomechanical resonators

Master's thesis in Nanotechnology

LAURENTIUS RADIT NINDITO

DEPARTMENT OF MICROTECHNOLOGY AND NANOSCIENCE
CHALMERS UNIVERSITY OF TECHNOLOGY
Gothenburg, Sweden 2024
www.chalmers.se

Master's thesis 2024

Tensile-strained crystalline aluminium nitride nanomechanical resonators

LAURENTIUS RADIT NINDITO

CHALMERS
UNIVERSITY OF TECHNOLOGY

Department of Microtechnology and Nanoscience
Quantum Technology Laboratory
Quantum Sensing and Foundations Lab
Chalmers University of Technology
Gothenburg, Sweden 2024

Tensile-strained crystalline aluminium nitride nanomechanical resonators

LAURENTIUS RADIT NINDITO

© LAURENTIUS RADIT NINDITO, 2024.

Supervisor: Anastasiia Ciers and Witlef Wieczorek, Department of Microtechnology and Nanoscience (MC2)
Examiner: Witlef Wieczorek, Department of Microtechnology and Nanoscience (MC2)

Master's Thesis 2024
Department of Microtechnology and Nanoscience
Quantum Technology Laboratory
Quantum Sensing and Foundations Lab
Chalmers University of Technology
SE-412 96 Gothenburg
Telephone +46 31 772 1000

Cover: A false-color SEM image of a phononically-shielded nanomechanical resonator realized on 90 nm crystalline aluminium nitride.

Typeset in LaTeX
Printed by Chalmers Reproservice
Gothenburg, Sweden 2024

Tensile-strained crystalline aluminium nitride nanomechanical resonators

LAURENTIUS RADIT NINDITO
Department of Microtechnology and Nanoscience
Chalmers University of Technology

Abstract

High-Q_m nanomechanical resonators have proven to be a promising platform for advancing quantum technology. Resonators with $Q_\mathrm{m} \times f_\mathrm{m}$ products exceeding 6.2×10^{12} Hz can sustain at least one coherent oscillation at room temperature, enabling their use in emerging quantum applications such as engineering long-lived quantum states and quantum sensing. Silicon nitride has become the favored material in this regard due to its great mechanical properties. However, it is an amorphous material that lacks additional functionalization capabilities beyond its admirable mechanical characteristics.

We therefore explore crystalline aluminum nitride (AlN) as a promising alternative platform for high-Q_m nanomechanical resonators. Like other crystalline nitride materials, we expect AlN to possess robust mechanical properties. Moreover, the lack of centrosymmetry in its crystal structure gives rise to its piezoelectricity, making it a particularly versatile material for electromechanical applications.

In this thesis, we studied four tensile-strained crystalline aluminum nitride samples with thickness ranging from 90 nm to 295 nm. We extracted their elastic properties, including Young's modulus, residual stress, and intrinsic quality factor. We then designed and realized phononically-shielded high-Q_m nanomechanical resonators out of them. Our best-performing device achieved a quality factor of 8.6×10^6 and a $Q_\mathrm{m} \times f_\mathrm{m}$ product as high as 1.5×10^{13}, sufficient to provide a coherent oscillation at room temperature.

Keywords: high-Q, quality factor, crystalline, aluminium nitride, aln, quantum, nano, mechanical resonator, soft clamping, phononic crystal, pnc, bangap.

Acknowledgements

With sincere gratitude, I would like to thank Prof. Witlef Wieczorek for giving me the opportunity to work in this rich and rewarding field as well as allowing me be part of his optomechanical team. A warm and sincere thank you to Anastasiia Ciers for guiding me through my daily struggles throughout the thesis period, without which I could not have completed this work. I am deeply grateful to Alexander Wolfgang Martin Jung and Hannes Pfeifer, from whom I have learned countless details about this new field. To all of the Quantum Sensing and Foundation Lab team: Karim Dakroury, Fabian Resare, Achintya Paradkar, Paul Nicaise, Hanlin Fang, Alireza Hashemi, and Somiya Islam Soke; I couldn't be more grateful for all the good times, laughs, and memories we shared together.

Lastly, I would like to express my deepest gratitude to my parents and my wife, to whom this thesis is dedicated.

Laurentius Radit Nindito, Gothenburg, December 2024

List of Acronyms

Below is the list of acronyms that have been used throughout this thesis listed in alphabetical order:

AlN	Aluminium nitride
f_{m}	Mechanical resonance frequency
PnC	Phononic crystal
Q_{m}	Mechanical quality factor

Contents

List of Acronyms **ix**

List of Figures **xiii**

List of Tables **xv**

1 Introduction **1**
1.1 Aim of this thesis 3
1.2 Thesis Organization 3

2 Theory **5**
2.1 Eigenfrequencies of a mechanical resonator 5
2.1.1 Continuum mechanics 5
2.1.2 Lumped-element model 7
2.2 Mechanical quality factor 8
2.2.1 Loss mechanisms 8
2.2.2 Loss minimizing strategies 10
2.3 Phononic crystal 12
2.3.1 Toy model of PnC's bandgap formation 13
2.3.2 PnC bandap engineering 13

3 Methods **15**
3.1 Simulation 15
3.2 Microfabrication 15
3.2.1 Detailed fabrication process 16
3.2.2 Film cracks and the chocolate bar method 17
3.3 Characterization 17
3.3.1 Homodyne detection 18
3.3.2 Ringdown 20

4 Material Characterization **21**
4.1 Young's modulus 21
4.2 Residual stress 23
4.2.1 Mechanical frequency method 24
4.2.2 Raman spectroscopy 26
4.3 Intrinsic quality factor 27
4.4 Summary 28

5 Results **29**
5.1 Design . . . 29
5.1.1 PnC unit cell bandgap simulation . . . 29
5.1.2 PnC defect engineering . . . 33
5.1.3 Membrane assembly . . . 34
5.1.4 Evaluation and optimization of mechanical quality factor . . . 35
5.1.4.1 Defect optimization . . . 36
5.1.4.2 Thickness dependence . . . 37
5.2 Fabrication . . . 37
5.2.1 Honeycomb PnC . . . 37
5.2.2 Snowflakes . . . 39
5.2.3 Dandelion . . . 39
5.3 Characterization . . . 40
5.3.1 Snowflake . . . 40
5.3.2 Dandelion . . . 41
5.4 Conclusion . . . 43

6 Conclusion and Outlook **45**

A Appendix A **51**
A.1 Simulation parameter . . . 51

List of Figures

1.1 The trend of the quality factor with the miniaturization of mechanical structures. . . . 2

2.1 Euler-Bernoulli beam model 6
2.2 A lumped-element model of a resonator 7
2.4 The plot of Q_{gas} of a square membrane resonator as a function of vacuum pressure 9
2.5 Curvature of the fundamental mode of a 170 µm-long uniform doubly-clamped beam 11
2.6 Soft clamping concept and realization 12
2.7 Concept of strain engineering 13
2.8 Toy model of PnC's bandgap formation 14

3.1 FEM-based eigenfrequency simulation 16
3.2 The microfabrication overview for AlN nanomechanical resonator 16
3.3 Standard and the chocolate bar method dicing 18
3.4 The homodyne detection setup 19
3.5 A typical result of the ringdown measurement 20

4.1 The typical shape of ductile materials' stress-strain characteristic 22
4.2 Cantilever resonators 22
4.3 Wafer bending and film stress 23
4.4 Film stress characterization via doubly-clamped beams 25
4.5 Film stress characterization via Raman spectroscopy 26
4.6 Intrinsic quality factor characterization 27

5.1 The three different PnC patterns 30
5.2 Band diagram of the fabricated PnC patterns 31
5.3 Relative bandgap of the three PnC patterns as a function of their crystal parameters 32
5.4 Defect geometry for each PnC pattern 33
5.5 The complete structures of the three PnC patterns and the displacements of their corresponding defect modes. 34
5.6 Diluted internal quality factor Q_{D} and radiative quality factor Q_{rad} as a function of the number of PnC unit cells for all three PnC patterns 35
5.7 Optimization of defect design for snowflake and dandelion PnC patterns . . . 36
5.8 Optical images of Honeycomb at different etching times 38
5.9 Simulation of the release process 38

5.10 Optical images of two successfully fabricated snowflake PnC devices on 295 nm-thick AlN films . . . 39
5.11 Optical and SEM images of fabricated Dandelion PnC devices . . . 39
5.12 Snowflake characterization result . . . 40
5.13 Characterization of the 295 nm dandelion PnC devices. . . . 41
5.14 Characterization of the 90 nm dandelion PnC devices . . . 42
5.15 Q_m of defect modes of 90 nm dandelion devices as a function of hexagonal hole diameter d_h. . . . 43
5.16 Summary of simulation and experimental results for all three PnC designs . . . 44

List of Tables

4.1 Calculated Young's modulus (E) for different thickness (h) of AlN films. . . 23
4.2 Film stress determined from mechanical frequency fitting of doubly-clamped beams . . . 25
4.3 Evaluation of released strain ($\epsilon_{\text{released}}$) and intrinsic quality factor (Q_{int}) as a function of AlN film thickness (h) . . . 27
4.4 Summary of elastic properties of different thicknesses of AlN film: Young's modulus, residual stress, and intrinsic quality factor . . . 28

5.1 Crystal parameters used in FEM simulations of the fabricated PnC patterns 30
5.2 Simulated results of f_{m}, Q_{m}, and $Q_{\text{m}} \times f_{\text{m}}$ for different AlN thickness . . . 37

A.1 Material properties of AlN used as parameters in FEM simulations 51

1

Introduction

Mechanical resonators are everywhere around us. From tiny trapped particles to massive suspended bridges, these objects can be seen as resonators - systems that oscillate at certain frequencies [1]. The motion of these objects stems from a non-zero net force that acts on them. For instance, at finite temperature, this motion arises from the thermal energy present in their environment [2]. We can analyze the oscillation of the resonator using the Fourier transform technique [3], which will decompose the resonator's seemingly random movement into vibrations of well-defined frequencies and amplitudes. These frequencies are called **eigenfrequencies** of the oscillator.

In mechanical structures the eigenfrequencies depend on material properties (e.g. elastic properties), geometry of the resonators, and forces acting on it [4]. Due to this fact, frequency shifts of a resonator can be utilized to probe changes in various physical quantities, such as force [5, 6], mass [7, 8], or displacement [9, 10].

Mechanical resonators come in vast variety of shapes and sizes (see Fig. 1.1). With the extraordinary advancements in the semiconductor industry there has been a growing trend toward developing mechanical resonator-based sensors in increasingly compact forms. This miniaturization enables these sensors to be seamlessly integrated into integrated circuits (IC), giving rise to devices such as microelectromechanical systems (MEMS) and nanoelectromechanical systems (NEMS). Yet, size and integration are not the only benefits here. The fundamental equations governing the resonator behavior tell us that scaling down a resonator also offers other benefits, i.e. increased frequency, reduced mass, and lowered thermal force noise, all of which improve its utility as a sensor [1, 2].

On the downside however, reducing the size of the resonator *used to* also lower a crucial resonator parameter known as the quality factor, Q_m (see Fig. 1.1). Fortunately, this situation changed with the discovery of high-Q_m nanostrings made from tensile stressed thin films two decades ago [11] and progress has been steadily advancing ever since.

If we pluck a guitar string, it will start to vibrate and produce a sound. Over time however, its vibrations will gradually fade and eventually stop. This occurs because the guitar string, like all vibrating systems, experiences energy loss; in other words, the mechanical excitation energy dissipates. There are various dissipation mechanisms and the magnitude of each mechanism's contribution depends on a large number of variables [1].

For sensing applications, the precision of a mechanical resonator-based sensor will be

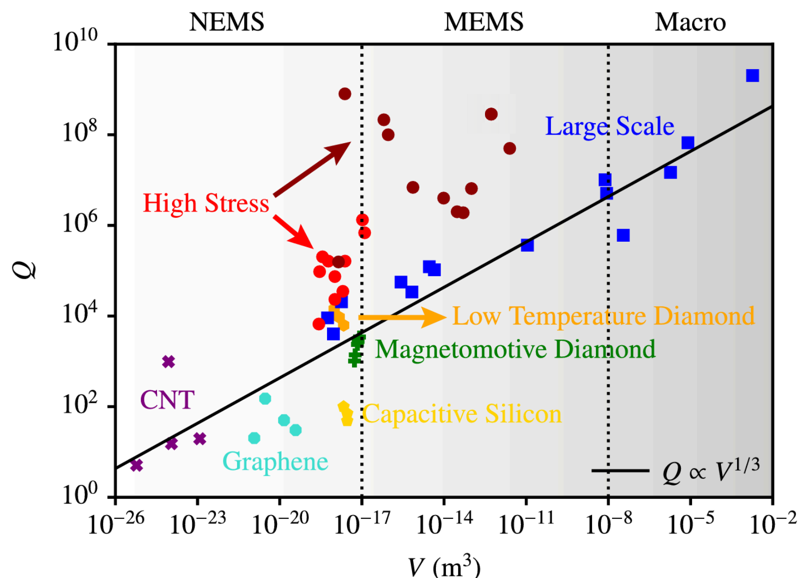

Figure 1.1: The trend of the quality factor with the miniaturization of mechanical structures. The black diagonal trend line illustrates that, for resonators without high stress, the quality factor scales proportionally to the cube root of their volume. However, high-stress mechanical resonators break this trend, enabling the realization of smaller volume resonators while achieving high quality factors. Figure taken from [12].

determined by how well we can resolve its frequency shift, which in turn, depends on its dissipation rate. In order to attain a high resolution of the frequency shift, the resonator is therefore required to possess a low loss rate [13]. The total dissipation rate of energy is often described via **the quality factor**, Q_{m}, which can be written as

$$Q_m = \Omega/\Gamma, \tag{1.1}$$

where Ω and Γ are the eigenfrequency and total energy dissipation rate of a mechanical resonator system, respectively. Intuitively, Q_{m} can be understood as a measure of how well a system is isolated from its environment, that limit both the dissipation of the system's energy into its surroundings as well as external noise sources from affecting/entering into the system. To achieve high-Q_{m} resonators, techniques such as acoustic isolation [14], soft clamping [15], dissipation dilution [16], and strain engineering [17] can be used.

Remarkable advancement in Q_{m} over the past decade have enabled mechanical resonators to be utilized not only for classical sensing applications but also, more intriguingly, in emerging quantum technology applications such as engineering long-lived quantum states [18] and in quantum sensing [19]. For these type of applications however, one not only needs to maximize Q_{m}, but also the $Q_{\mathrm{m}} \times f_{\mathrm{m}}$ product. This is because a fundamental requirement for such applications would be that the utilized resonator must be able to perform at least one coherent oscillation before a single phonon from the environment can enter the system, which is expressed mathematically as [20]

$$Q_\mathrm{m} \times f_\mathrm{m} > \frac{k_B T}{h}, \tag{1.2}$$

where f_m is the mechanical frequency of the system, k_B is the Boltzmann constant, T is the temperature, and h is Planck's constant. At room temperature, $\frac{k_B T}{h}$ is equal to 6.2×10^{12} Hz. Recently it has been demonstrated that a key ingredient in realizing high $Q_\mathrm{m} \times f_\mathrm{m}$ product is using nanometer-thin, highly stressed films [15, 17, 21], with silicon nitride (SiN) emerging as the go-to material, that reached Q_m of 10^9 and $Q_\mathrm{m} \times f_\mathrm{m}$ product of 10^{15} at 6 K temperature [21].

From both performance and fabrication perspectives, SiN offers numerous advantages, making it a highly desirable material. However, its amorphous nature introduces inherent challenges, as defects are distributed throughout the material, leading to intrinsic loss [22]. Furthermore, the absence of a crystalline lattice limits its functionalities, restricting its potential applications.

Efforts have focused on exploring various crystalline materials, such as silicon carbide (SiC) [23, 24], indium gallium phosphide (InGaP) [25], and silicon (Si) [26]. At the moment, the state-of-the-art record is hold by 14 nm-thick strained Si resonators that reach Q_m of 10^{10} and $Q_\mathrm{m} \times f_\mathrm{m}$ of 10^{16} Hz at 7 K temperature [26]. One major advantage of crystalline over amorphous materials is that their crystal structure can give rise to many interesting phenomena, such as superconductivity [27], piezoelectricity [28], magnetism, etc. Unfortunately, crystallinity in silicon doesn't give any added benefit other than robust mechanical properties.

1.1 Aim of this thesis

In this thesis, we explore a new direction by investigating crystalline aluminum nitride (AlN) films to develop high $Q_\mathrm{m} \times f_\mathrm{m}$ product nanomechanical resonators. Like other crystalline nitride materials, AlN exhibits robust mechanical properties and excellent chemical stability. Additionally, the lack of inversion symmetry in its crystal structure introduces piezoelectricity, providing an additional electric degree of freedom for further functionalization.

Specifically, we aim to design, simulate, fabricate and characterize high-Q nanomechanical resonators utilizing epitaxially grown aluminum nitride on silicon. A soft clamping technique, known as phononic crystal engineering, will serve as the primary approach for achieving a high mechanical quality factor. As a key measurable objective, their $Q_\mathrm{m} \times f_\mathrm{m}$ would need to surpass 6.2×10^{12} Hz for the fabricated resonators to enter the quantum regime at room temperature.

1.2 Thesis Organization

This thesis consists of six chapters.

The introduction (chapter 1) provides background information of the core topic of this thesis, as well as discusses the state-of-the-art achievement in the field of nanomechanical resonators.

The theory (chapter 2) provides an overview of the fundamental concepts behind understanding nanomechanical resonators that are utilized throughout this thesis.

The method (chapter 3) elaborates on the methods of design and fabrication throughout the thesis.

The material characterization (chapter 4) discusses the characterization of the material properties of the aluminum nitride thin films used in this study.

The result (chapter 5) presents the results from the design, fabrication, and characterization of the phononically-shielded nanomechanical resonators realized in aluminium nitride.

The conclusion and outlook (chapter 6) offers final remarks and insights gained throughout this work.

2

Theory

This chapter presents essential concepts of nanomechanical resonators serving as the foundation for this thesis. It begins by introducing the concept of eigenfrequencies of mechanical resonators. The discussion continues with the elaboration of the mechanical quality factor, as well as techniques to maximize its value. The chapter ends with an exploration of the concept of phononic crystals for increasing Q_{m}.

2.1 Eigenfrequencies of a mechanical resonator

Eigenfrequency refers to the inherent natural frequency at which a structure vibrates without any energy dissipation. In this section, two models of mechanical resonator, i.e. continuum mechanics and lumped-element model, will be used be able to describe its motion.

2.1.1 Continuum mechanics

For small deformations, a mechanical resonator is considered to be an elastic continuum mechanical structure, meaning a continuous object with the ability to return to its original shape after being deformed. There are many ways mechanical resonators can vibrate, which we refer to as vibrational modes. Each of these modes corresponds to a specific eigenfrequency and vibrational pattern. To determine the eigenfrequency of a mechanical resonator, we therefore need to first identify these vibrational modes which can be done by constructing and solving the mechanical resonator's equation of motion.

Consider for example a resonator in the shape of a beam (see Fig. 2.1). Under the assumption that the beam is slender (length $\gg$ thickness) and the rotational inertia and shear deformation can be neglected, the equation of motion of this beam takes the form of the Euler-Bernoulli equation [29]

$$\rho A \frac{\partial^2 u(x,t)}{\partial t^2} + \underbrace{EI_y \frac{\partial^4 u(x,t)}{\partial x^4}}_{\text{bending}} - \underbrace{\sigma A \frac{\partial^2 u(x,t)}{\partial x^2}}_{\text{elongation}} = 0, \tag{2.1}$$

where $u(x,t)$ is the beam's displacement as a function of position x and time t, ρ is the mass density, A is the cross-sectional area, E is Young's modulus, I_y is the geometric moment of inertia with respect to the y-axis, and σ is film stress.

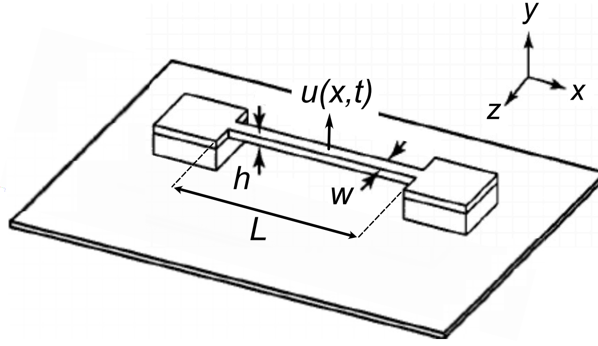

Figure 2.1: Euler-Bernoulli beam model, with length L, width w, and thickness h, clamped at both ends. The displacement $u(x,t)$ indicates the oscillation direction of the beam as a function of position x along the beam's length and time t. Adapted from [31]

For the different cases, there are different derivations and solutions to this equation which can be found in textbooks, e.g. Ref. [30]. The case we are particularly interested in is the free vibrations of a tensile-stressed beam, for which the bending term is much smaller than the elongation term, thus can be neglected. The boundary condition for a tensile-strained and doubly-clamped beam is

$$U_n(0) = U_n(L) = \frac{\partial^2}{\partial x^2}U_n(0) = \frac{\partial^2}{\partial x^2}U_n(L) = 0. \tag{2.2}$$

Assuming a sinusoidal mode shape with wavenumber β

$$U_n(x) = \sin(\beta_n x), \tag{2.3}$$

the general solution (eigenmodes) can be written as

$$u(x,t) = \sum_{n=1}^{\infty} U_n(x)\cos(\Omega_n t). \tag{2.4}$$

where Ω_n are the corresponding eigenfrequencies and n denotes the modal number. By choosing wavenumbers that satisfy the boundary condition ($\beta_n = \frac{n\pi}{L}$), the n-th eigenfrequency is

$$\Omega_n = \frac{n\pi}{L}\sqrt{\frac{\sigma}{\rho}}. \tag{2.5}$$

Eq. 2.5 shows that the eigenfrequency of a stressed beam is proportional to the square root of the stress and inversely proportional to the length. This insight is a handy takeaway to keep in mind as it also appears in the eigenfrequency formulas for other stressed 2D membranes as well as in the dissipation dilution formula introduced later on.

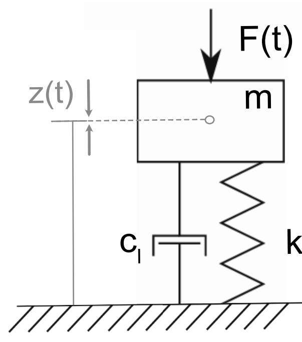

Figure 2.2: A lumped-element model of a resonator, consisting of a mass m, a spring with spring constant k_l, a damper with damping coefficient c_l, and a sinusoidal-profiled external force $F(t)$. The position of the mass in the z-direction is denoted as $z(t)$. Adapted from [1].

2.1.2 Lumped-element model

The lumped-element model is a method for simplifying a complex system by representing its overall behavior using a single element, or 'lump'. The lumped-element model for mechanical systems consists of four components, shown in Fig. 2.2: mass (m), spring constant (k_l), damping coefficient (c_l), and external force ($F(t)$). They represent the effective inertia, the effective restoring force, energy dissipation, and any external forces acting on the object of interest, respectively.

The equation of motion for the lumped element model can be written as

$$m\frac{d^2z(t)}{dt^2} + c_l\frac{dz(t)}{dt} + k_l z(t) = F(t). \tag{2.6}$$

There are three important cases to consider [30]:

1. **Free undamped vibration** refers to the mechanical system that vibrates without energy loss or external forces acting upon it ($c_l = 0,\ F(t) = 0$). In this case, the energy stored within the system remains constant, and the system will oscillate indefinitely at the eigenfrequency $\Omega = \sqrt{k_l/m}$.

2. **Free damped vibration** refers to the mechanical system that vibrates without any external force, but with energy loss present ($c_l \neq 0,\ F(t) = 0$). In this scenario, the system will experience gradual energy dissipation resulting in exponential decay of its oscillation amplitude over time. Two important metric related to this dissipation are the damping ratio $\zeta = \frac{c_l}{2\sqrt{mk_l}}$ and the damping rate $\Gamma = 2\zeta\Omega$. In Fig. 2.3a one can see that on the harmonic function we get an exponentially decaying envelope at a rate $\frac{\Gamma}{2}$. An important parameter to characterize damped mechanical oscillators is the quality factor Q_m, as it describes the number of cycles the oscillator undergoes before the amplitude decays to 1/e of its initial value (more on Sec. 2.2). This definition translates to $Q_m = \frac{\Omega}{\Gamma} = \frac{1}{2\zeta}$.

3. **Driven damped vibration** refers to the mechanical system in which both energy

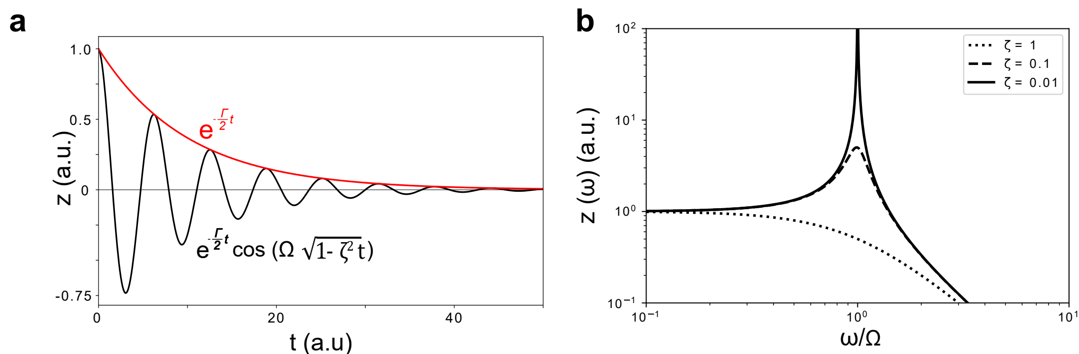

Figure 2.3: Response of a damped harmonic oscillator. (a) Without an external force, $z(t)$ shows an exponentially decaying oscillation with an envelope $e^{-\frac{\Gamma}{2}t}$. (b) With the presence of an external force, the system's frequency response $z_0(\omega)$ shows the presence of resonance peaks that vary with damping coefficient.

loss and an external force are present ($c_l \neq 0$, $F(t) \neq 0$). The solution to Eq. 2.6 in frequency space is given as

$$z(\omega) = \frac{F(\omega)}{m} \frac{1}{\Omega^2 - \omega^2 + i\omega\Gamma} \tag{2.7}$$

As plotted in Fig. 2.3b, the equation shows that the presence of an external force with frequency close to the eigenfrequency induces an amplitude magnifying phenomenon that we call resonance, provided the damping ratio is low.

2.2 Mechanical quality factor

The mechanical quality factor (Q_m) serves as a metric to quantify how well a resonator is isolated from its environment, essentially representing the inverse of the total dissipation occurring in the given system. Q_m is defined as

$$Q_\mathrm{m} = 2\pi \frac{W}{\Delta W}, \tag{2.8}$$

where W represents the total stored energy in the system, and ΔW represents energy that is lost per oscillation cycle.

2.2.1 Loss mechanisms

Mechanical resonators can lose their energy through numerous different mechanisms. Three main energy loss mechanisms specified in this work are gas damping, phonon tunneling loss, and intrinsic loss, which correspond to the gas-limited quality factor Q_gas, radiation-loss-limited quality factor Q_rad [32], and intrinsic quality factor Q_int [33], respectively. The overall mechanical losses add up incoherently, thus Q_m can be written as

$$\frac{1}{Q_\mathrm{m}} = \Sigma \frac{1}{Q_i} = \frac{1}{Q_\mathrm{gas}} + \frac{1}{Q_\mathrm{rad}} + \frac{1}{Q_\mathrm{int}} + \frac{1}{Q_\mathrm{other}}. \tag{2.9}$$

Gas damping arises from the interaction between mechanical resonators and the surrounding gas molecules, which can be viewed as behaving like a viscous medium. When a resonator vibrates, it displaces the gas around it. As the gas molecules collide with the resonator's surface, momentum transfer occurs from the resonator to the surrounding gas, resulting in the dissipation of the resonator's energy.

When a mechanical resonator placed in vacuum with pressure that corresponds to the so-called Knudsen number $Kn > 1$, it can enter the ballistic regime where gas molecules travel distances comparable to or longer than the characteristic dimensions of the resonator without colliding, resulting in reduced damping due to fewer gas molecule-resonator collision. In this regime, Q_{gas} for a square membrane resonator is [34]

$$Q_{\mathrm{gas,\ sq}}(p) = \frac{\rho h \omega}{4}\sqrt{\frac{\pi}{2}}\sqrt{\frac{R_{\mathrm{gas}}T}{M_{\mathrm{m}}}}\frac{1}{p}, \tag{2.10}$$

where ρ is material density, h membrane thickness, ω is the angular velocity of the oscillation, T is temperature, M_{m} is molar mass of the gas, R_{gas} is the universal molar gas constant. The Knudsen number itself is defined as

$$Kn = \frac{\lambda_f}{L_r} \tag{2.11}$$

where λ_f is the mean free path length of the gas, and (L_f) is a representative length scale of the resonator.

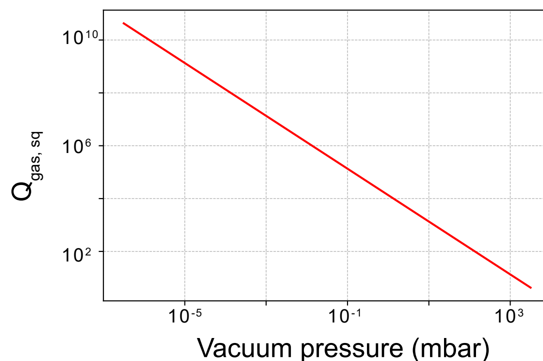

Figure 2.4: The plot of Q_{gas} of a square membrane resonator as a function of vacuum pressure, illustrating how Q_{gas} increases linearly as the vacuum pressure decreases.

Fig. 2.4 shows the evaluation of Eq. 2.10 for a square membrane resonator made from 300 nm-thick AlN film oscillating at 1 MHz at varying gas pressures. At atmospheric pressure (10^3 mbar) Q_{gas} is ~10, which will limit the total mechanical quality factor of the resonator. Fortunately, this condition can be easily improved by reducing the gas pressure, by using a high vacuum (~10^{-7} mbar) or even an ultra-high vacuum chamber ($< 10^{-7}$ mbar) to perform the study of high-Q mechanics.

Phonon tunneling loss is a type of loss that happens when phonons from a resonator propagate out into the substrate through its clamping points. The formula for Q_{rad} for a square-shaped membrane is [1, 35]

$$Q_{\mathrm{rad,sq}} = 1.5\frac{\rho_s}{\rho_r}\eta^3\frac{n^2m^2}{(n^2+m^2)^{3/2}}\frac{L}{h}, \tag{2.12}$$

with ρ_s and ρ_r are the mass densities of the substrate and resonator, n and m are n-th and m-th eigenmodes of the substrate and resonator. Acoustic mismatch η can be approximated by $\sqrt{\frac{E_{\mathrm{s}}\rho_{\mathrm{r}}}{\rho_{\mathrm{s}}\sigma}}$, where E_{s} refers to the Young's modulus of the substrate and σ is stress of the resonator.

$Q_{\mathrm{rad,sq}}$ for 300 nm AlN film on silicon with $n, m = 1$ is 1.5×10^6. To evaluate Q_{rad} for a particular resonator design however, can be tricky as it highly depends on the exact design of the clamping points, making Eq. 2.12 no longer applicable. Therefore, Q_{rad} is typically evaluated using finite element method (FEM) simulations.

Intrinsic loss is an umbrella term that encompasses various types of losses that can occur within the resonator itself, such as [30]

1. friction loss, which is associated with the time lag between the propagation of strain and stress within the material,
2. thermoelastic damping (TED), which arises due to the coupling between thermal and elastic effects within the resonator,
3. Akhiezer damping, which occurs due to the interaction between phonons within a material when it is deformed.

The overall value of Q_{int} can vary significantly between different materials. Therefore, Q_{int} needs to be determined experimentally.

2.2.2 Loss minimizing strategies

Several techniques to reduce mechanical loss have been developed in recent years, with the most notable ones being dissipation dilution [36, 16], soft clamping [15], and strain engineering [17].

Dissipation dilution is a phenomenon of Q_{m} enhancement in mechanical resonators due to the tensile stress of its material. The key secret of this boost is that a tensile stressed material provides a lossless energy storage medium in the form of tensile potential energy. It has been shown in [36] that Q_{m} of a tensile stressed beam can be modeled as

$$Q_{\mathrm{D}} = D_{\mathrm{Q}}Q_{\mathrm{int}}, \tag{2.13}$$

where Q_{D} is the diluted internal quality factor and D_{Q} is the dissipation dilution factor, which furthermore can be written as

$$D_{\mathrm{Q}} = 1 + \frac{U_{\mathrm{elongation}}}{U_{\mathrm{bending}}}, \tag{2.14}$$

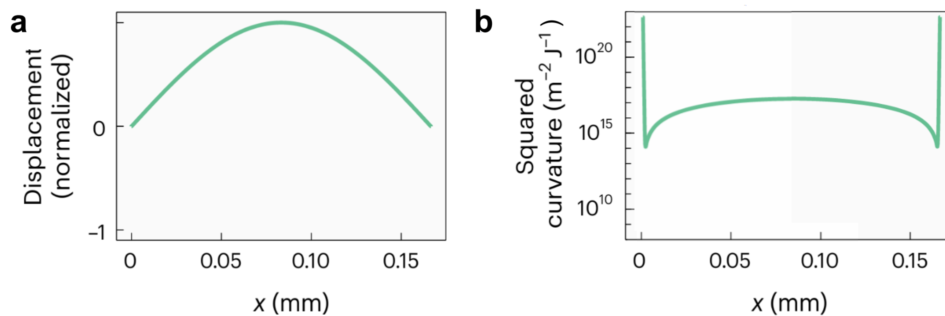

Figure 2.5: Curvature of the fundamental mode of a 170 µm-long uniform doubly-clamped beam. (a) The displacement profile as a function of position along its length, normalized to its maximum displacement. (b) The square of its curvature normalized to the kinetic energy, signify the magnitude of bending loss at its clamping points. Figure taken from [38].

with $U_{\text{elongation}}$ and U_{bending} are the total potential energy stored in beam's elongation and bending, respectively. As $U_{\text{elongation}} \gg U_{\text{bending}}$ in tensile stressed beams, D_{Q} becomes much greater than unity and thus enhances Q_{m}. If we see it from the opposite side, D_{Q} 'dilutes' the internal loss mechanisms present within the resonator, hence the name.

Through further derivation, D_{Q} for beams is given as [16]

$$D_Q^{\text{beam}} = \left[\underbrace{2\lambda}_{\text{edge shape}} + \underbrace{(n\pi)^2\lambda^2}_{\text{sine shape}} \right]^{-1}, \tag{2.15}$$

where the stress parameter $\lambda = \frac{h}{L}(\frac{E}{12\sigma})^{1/2}$. In high aspect ratio mechanical resonators made from thin films, λ is significantly less than 1, making the edge shape term significantly bigger than the sine shape term.

This key insight is well-captured in Fig. 2.5b, which shows the evaluation of the normalized squared curvature of the fundamental mode of a doubly-clamped beam, representing the magnitude of bending loss present at each point along its length. The main takeaway from the plot is that bending loss at the edges is several orders of magnitude higher compared to any other point within the structure.

Since this issue has been identified, significant efforts have been put to overcome it, leading to new resonator designs such as hierarchical structures [21] or perimeter modes [37].

Soft clamping is a technique aimed at eliminating the hard clamping point between the resonator and its substrate. This approach involves designing a resonator in such a way that can shift its motional amplitude away from the edges, leaving the clamping points with minimal vibration (see Fig. 2.6b).

The way to realize this concept is through the utilization of phononic crystals which create a so-called phononic bandgap (see Sec. 2.3). A defect, or a pattern different from those of

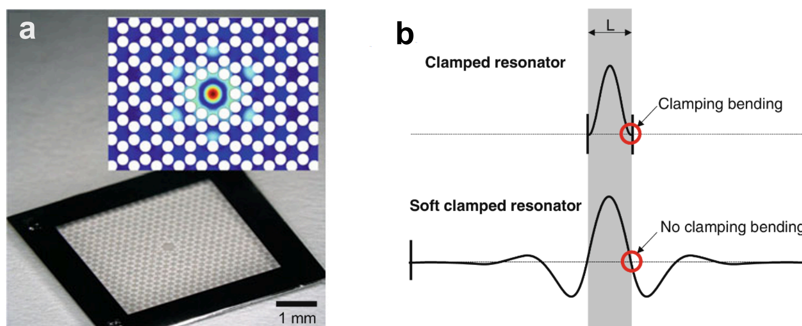

Figure 2.6: Soft clamping concept and realization. (a) A realization of a soft clamped mechanical resonator utilizing phononic crystal structure, with an inset illustrating the simulated displacement of the localized defect mode. (b) Illustration of soft clamping concept, demonstrating a soft decaying vibration amplitude toward the edge, avoiding the formation of hard clamping points. Taken from [30].

the phononic crystal pattern, is then placed within it. This arrangement creates a localized vibrational mode as the phononic bandgap reflects phonons of the defect mode entering its structure, resulting in a soft decaying amplitude of defect mode vibration towards the edge. This phenonenon gives two fold benefits: (i) Q_{D} enhancement by substantially decreasing bending at the clamping point (ii) Q_{rad} enhancement by practically eliminating phonon tunneling loss [1].

Strain engineering is a technique used to enhance the performance of resonators by controlling the strain (ϵ) distribution within the material. The core idea is to engineer the strain to be in areas where the most significant bending—and therefore the highest energy loss—occurs. From Eq. 2.15, λ is proportional to the square root of $\frac{E}{\sigma}$, or in other words, the square root of strain. By increasing the strain in the high-loss regions, we effectively enhance the dissipation dilution locally there.

This concept is implemented in [17] in the form of a tapered highly stressed soft-clamped phononic crystal beam (see Fig. 2.7). This demonstrates that by tapering the beam, the strain can be redistributed based on the geometry of the beams, creating a region of locally enhanced strained in the center of the beam. This strain focusing aligns with where the defect mode is localized. The enhancement in the $Q_{\mathrm{m}} \times f_{\mathrm{m}}$ product is significant, allowing the beam to reach a performance that would not be achievable with soft clamping alone.

2.3 Phononic crystal

A phononic crystal (PnC) is a repeating structural pattern that exhibits periodic variations in effective elastic properties. The periodic elastic properties are the crucial factor that gives rise to the phononic bandgap. A phononic bandgap can roughly be described as a range of frequencies within which acoustic or elastic waves are unable to propagate through. This phenomenon has attracted significant research interest and has been exploited in many different applications, such as in the realization of soft clamping in nanomechanical resonators [15] or PnC mirrors [19].

PnCs are made up of unit cells, the smallest repeating structures that define the phononic

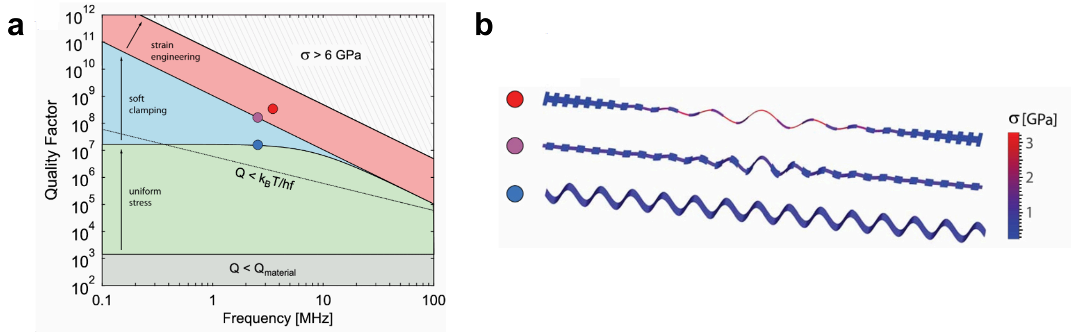

Figure 2.7: Concept of strain engineering. (a) Theoretical quality factor achievable using 20 nm thick SiN beams using three different design strategies: strain engineering, soft clamping, and uniform stress. (b) Three mode shapes representing strain engineering (red dot), soft clamping (purple dot) and uniform stress (blue dots). The color on the mode shapes represents the film stress. Taken from [17].

crystal overall structure. In the context of a nanomechanical resonator, these unit cells can be arranged in one-dimensional or two-dimensional configurations, enabling the control of wave propagation in those respective dimensions.

2.3.1 Toy model of PnC's bandgap formation

To provide a more intuitive understanding of the underlying physics, we can represent a PnC using a toy model of spring and mass chains. Consider an infinite chain of two alternating masses, denoted as m_1 and m_2, connected by a spring with a spring constant k_s, as shown in Fig. 2.8. For such a system, its dispersion can be written as [36]

$$\Omega_{\pm} = \sqrt{(\Omega_1^2 + \Omega_2^2) \pm \sqrt{(\Omega_1^2 + \Omega_2^2)^2 - 4\Omega_1^2\Omega_2^2 \sin^2(k/2)}}, \tag{2.16}$$

where Ω_+ and Ω_- are the upper and lower bound frequency of Fig. 2.8, $\Omega_1 = \frac{k_s}{m_1}$, $\Omega_2 = \frac{k_s}{m_2}$ are the natural resonance frequency of each mass, and k is an angular frequency in the wave propagation direction. Eq. 2.16 tells us that if m_1 is different from m_2, then Ω_1 and Ω_2 would also be different, which leads to the formation of a bandgap, depicted as a gray area in the band diagram. The width of the bandgap ($\Delta\Omega_B$) is given by

$$\Delta\Omega_B = \sqrt{2}|\Omega_1 - \Omega_2|. \tag{2.17}$$

2.3.2 PnC bandap engineering

In a real material, the periodic structure of the crystal lattice dictates how phonons can propagate within it. For a given crystal periodicity, phonons can only have momentum within a specific range of values. The key to determining this range of momentum values lies in the first Brillouin zone, which is the fundamental region in reciprocal space containing all unique wave vectors (k) that reflect the periodicity of the crystal. Within this zone, phonons can propagate through the crystal, whereas outside this range, the momentum

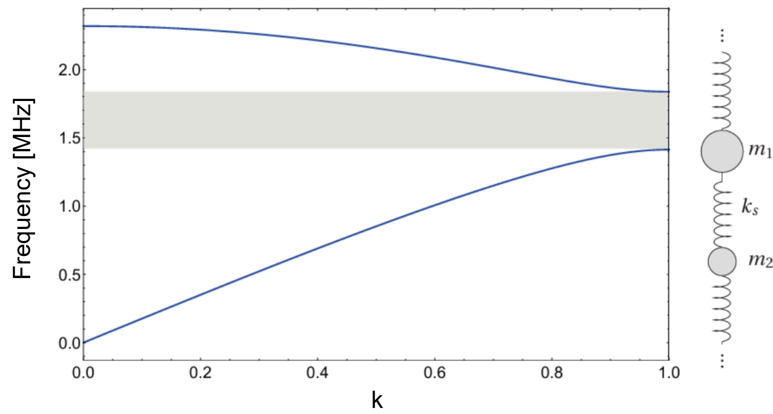

Figure 2.8: Toy model of PnC's bandgap formation. A dispersion relation for an infinite chain of alternating masses m_1 and m_2 connected by springs with a spring constant k_s (shown by the schematic on the right). The gray area depicts the bandgap, a region where phonon propagation is not allowed. A phonon entering it will get exponentially damped. Taken from [36].

values are not allowed. The construction of the Brillouin zone can be found in numerous references, e.g, Ref. [39, 40].

Once this range of momentum values are known, a band diagram can be constructed by evaluating the dispersion relation, which can be done using FEM simulation software. The obtained band diagram can then reveal whether or not a bandgap is present.

3

Methods

The realization of nanomechanical resonators comprise three major parts: simulation, microfabrication, and characterization. This chapter elaborates on the steps involved in each of them.

3.1 Simulation

We design our resonators through a four-step process:

1. PnC unit cell bandgap simulation, to identify a PnC unit cell that exhibits a bandgap within the MHz frequency range,
2. PnC defect engineering, to engineer a defect with a mechanical resonance frequency that lies within this bandgap,
3. Complete PnC nanomechanical resonator assembly, to assemble the two parts into the final 2D PnC membrane design, and
4. Evaluation and optimization of f_m and Q_m.

In performing all the steps, the eigenfrequency study in Comsol Multiphysics serves as our FEM-based simulation tool, which identifies vibrational modes and their corresponding frequencies from a given input structure (see Fig. 3.1). It works by conducting a two-step simulation process: a stationary analysis that determines the stress distribution within the structure based on a given initial stress, and then the eigenfrequency analysis that computes the eigenmodes using the stress distribution information from the static analysis result. This approach allows Comsol to accurately determine the resonance frequency of an arbitrary-shaped structure. For the evaluation of Q_m, we incorporate the formula of both the diluted internal quality factor (Eq. 2.13) and the dissipation dilution factor (Eq. 2.14) directly into the simulation.

3.2 Microfabrication

The overview of the microfabrication process is shown in Fig. 3.2: the AlN chip first undergoes a SiO_2 hard mask sputtering deposition, followed by a resist spin-coating process. Electron-beam lithography is then performed to pattern the resist layer with the desired resonator design. This pattern is transferred into the hard mask and then into the AlN film through ICP-RIE. Finally, the remaining resist and SiO_2 hard mask are removed, and the chip undergoes a dry XeF_2 release process to etch the silicon substrate beneath the AlN film.

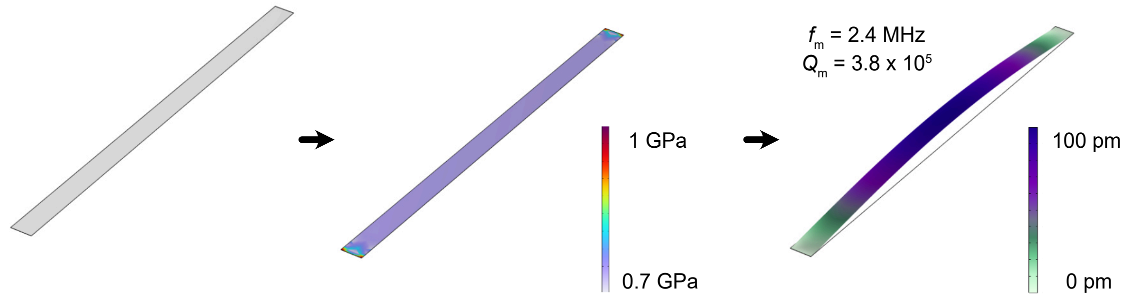

Figure 3.1: FEM-based eigenfrequency simulation, performed on the input geometry (left) in two sequential steps: a static simulation (middle) to determine the stress distribution within the structure based on a given initial stress, and the eigenfrequency simulation (right) that computes the eigenmodes as well as the corresponding Q_{m}.

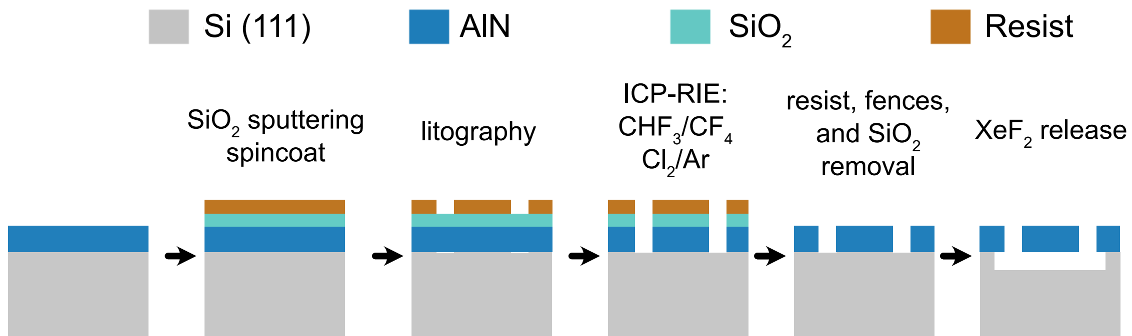

Figure 3.2: The microfabrication overview for AlN nanomechanical resonator, which consists of SiO_2 deposition, lithography, ICP-RIE, hard mask removal, and XeF_2 release processes.

3.2.1 Detailed fabrication process

Dicing. Wafer dicing is the first step in our fabrication workflow. This is because, while the AlN wafer has a diameter of 2 inches, our work focuses on millimeter-sized chips. Thus, the wafer is diced into smaller chips, typically measuring 10 mm × 7 mm or 7 mm × 5 mm.

Hard mask. Cl_2 gas will be used as the primary etchant for AlN. The resist we use is too thin to withstand the entire etching process. To address this issue, we sputtered a SiO_2 layer onto the AlN film to serve as a hard mask.

Resist coating and Electron-Beam Lithography (EBL). The next step in the fabrication process is the resist spin-coating. We use UV60 (3k rpm, 60s; pre-bake 130°C, 60s) as the resist and Ti-suspension (Ti-prime, 4k rpm, 20s; pre-bake 120°C, 120s) as the adhesive layer beneath it. UV60 is selected for its high resolution and fast exposure time. The patterning is performed using the EBL Raith EBPG 100 kV system (23 µC/cm^2, 5nA). Following lithography, secondary exposure (130°C, 60s) and development (MF-CD-26, 75s) are carried out immediately .

Inductively Coupled Plasma Reactive Ion Etching (ICP-RIE). At this stage, the pattern of our design is already transferred onto the resist but not yet onto the AlN thin-film. To transfer the pattern into the hard mask and AlN film, a dry-etching process is performed using an ICP-RIE tool. The process is carried out in two stages: first, the pattern is transferred to the SiO_2 hard mask using a mix of CF_4 and CHF_3 gases (30 sccm/20 sccm), and second, the pattern is transferred to the AlN thin film using Cl_2/Ar (30 sccm/15 sccm).

Resists, fences, and hard masks removal. Before the final releasing step, the remaining resist, fences and hard mask must be removed. First, the resist is removed using Remover-1165 (85°C, 300s) followed by oxygen plasma treatment (100W, 180s). Second, the fences—redeposited amorphous AlN on the sidewalls of the etched profile formed during the ICP-RIE step—are etched away using MF-CD-26 (120s)[1]. Finally, the SiO_2 hard mask is removed using an HF solution (2%, 90s).

XeF_2 release. The final step of the fabrication is the dry etch-release. We used XeF_2 etchant (whose concentration is determined by the nitrogen and hydrogen gas pressure and flow rates; $N_2 = 25$ sccm, $H_2 = 25$ sccm, $p = 1.2$ torr), that can perform an isotropic etch of the silicon substrate beneath the AlN thin film with excellent selectivity [41].

3.2.2 Film cracks and the chocolate bar method

During the dicing process, some AlN wafers experience severe cracking issues caused by chipped edges formed during the dicing (Fig. 3.3b). These localized cracks subsequently propagate across the samples during the release process, following the hexagonal lattice structure of the AlN film, resulting in cracks oriented at 120° angles relative to one another (Fig. 3.3a).

To address this issue, we implemented the so-called chocolate bar method, as detailed in [42]. The core idea here is to segment the whole AlN wafer into discrete rectangular patterns with some separation distance, typically 50-100 µm, which makes them look like a chocolate bar. This design allows the dicing saw to cut directly through the silicon substrate without contacting the AlN film (Fig. 3.3c), ensuring that the AlN remains untouched during the dicing process. As a result, crack formation during dicing is effectively prevented (Fig. 3.3d).

3.3 Characterization

Several tools were used to perform device and wafer characterization in this thesis, such as an optical microscope (Olympus MX50) to take images, scanning electron microsocpy (Zeiss Supra 55) to measure the actual dimension of our fabricated devices, ellipsometer (J.A. Woollam RC2) to measure the film thickness, and a Raman microscope (WITec alpha300 R) to determine the film stress. The primary characterization tools used to evaluate both the resonance frequency and mechanical quality factor of the fabricated nanomechanical resonators is the homodyne detection setup, as shown in Fig. 3.4.

[1] Amorphous AlN can be dissolved using base, such as KOH or TMAH.

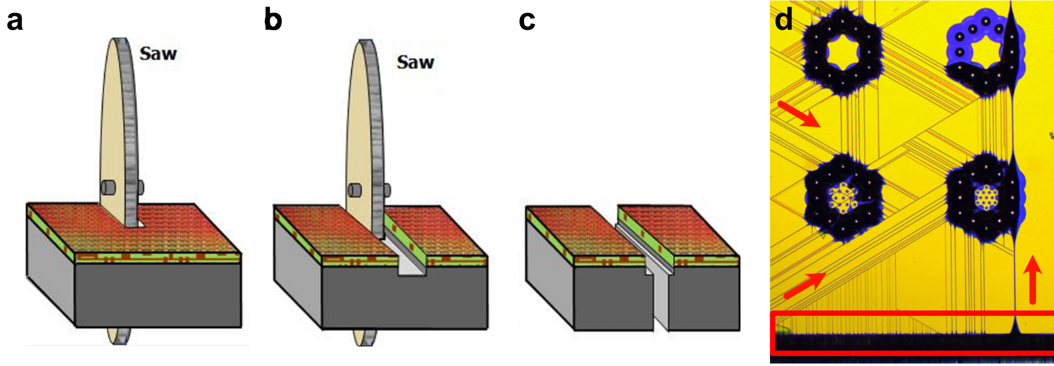

Figure 3.3: Standard and the chocolate bar method dicing. (a) Standard dicing process where the saw comes into contact with the AlN film. (b) Dicing process of the chocolate bar method, where the saw is positioned within the pre-made trench, allowing it to directly access the silicon substrate. (c) The pristine edge of the AlN film is preserved and crack formation is prevented. (d) Cracks in the AlN film originating from chipped edges formed during the dicing process (red rectangle), propagate along the crystal lattice during the release process (red arrows). Adapted from [42].

3.3.1 Homodyne detection

Homodyne detection is a highly sensitive technique used to extract an amplitude or phase information from a weak optical signal. It operates on the principle of mixing a weak signal beam with a strong reference beam, known as the local oscillator (LO), to produce an interference signal. This interference signal is detected using balanced detection, and the resulting signal is processed by a signal analyzer, which applies a Fourier transform to analyze and resolve the frequency components of the signal (see Fig. 3.4). To gain a deeper understanding of how this setup can be utilized for precise displacement measurements, it is essential to explore the governing equations that describe its operation.

Suppose we denote the time-dependent displacement of the fabricated resonator as Δx. When the laser beam from the signal arm, with a steady-state amplitude $\alpha_s(t)$, is reflected by the resonator surface, the displacement of the resonator causes a modulation in the phase quadrature of the signal beam. The resulting amplitude and phase fluctuations are represented by $\delta X_s(t)$ and $\delta Y_s(t)$, respectively, and can be expressed as [43, 44]:

$$\alpha_{\mathrm{s}}(t) = \alpha_{\mathrm{s}} + \delta X_{\mathrm{s}}(t) + i\delta Y_{\mathrm{s}}(t), \tag{3.1}$$

In a similar way, the laser beam in the LO arm can be written as

$$\alpha_{\mathrm{LO}}(t) = [\alpha_{\mathrm{LO}} + \delta X_{\mathrm{LO}}(t) + i\delta Y_{\mathrm{LO}}(t)]e^{i\varphi}, \tag{3.2}$$

where φ represents the phase difference between the signal arm and the local oscillator arm. Subsequently, the two signals are combined and mixed at the 50:50 beam splitter, resulting in the beams detected by the photodetectors (denoted as PD1 and PD2) being expressed as

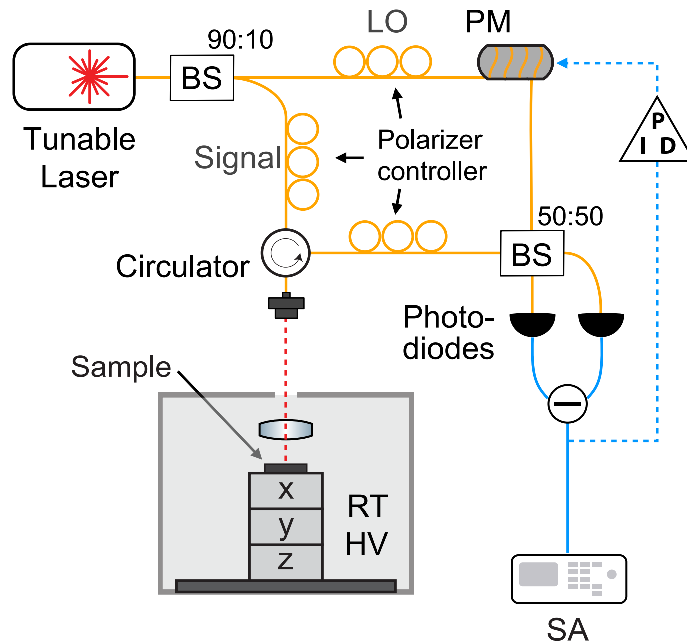

Figure 3.4: The homodyne detection setup, consists of a tunable telecom laser source (1510-1620 nm), generating a laser beam that is split into the signal and local oscillator (LO) arms by a 90:10 beam splitter (BS). In the signal arm, the beam is directed through a circulator to interact with the sample placed in a room-temperature high-vacuum (RT HV) chamber with XYZ position control. In the LO arm, the beam passes through a phase modulator (PM) before being recombined with the reflected signal beam at a 50:50 beam splitter. The resulting interference is measured by balanced photodiodes and analyzed using a spectrum analyzer (SA). A feedback signal is sent to a PID controller to achieve phase lock control. Polarizer controllers are placed in both the signal and LO arms to adjust the beam polarization. Adapted from [43].

$$\alpha_{\mathrm{D1}}(t) = \sqrt{\frac{1}{2}}\alpha_{\mathrm{LO}}(t) + \sqrt{\frac{1}{2}}\alpha_{\mathrm{s}}(t) \tag{3.3}$$

$$\alpha_{\mathrm{D2}}(t) = \sqrt{\frac{1}{2}}\alpha_{\mathrm{LO}}(t) - \sqrt{\frac{1}{2}}\alpha_{\mathrm{s}}(t) \tag{3.4}$$

Since the beam amplitude from the LO arm is much stronger than that from the signal arm, the difference in intensity between the two photodetectors can be expressed as [45]:

$$i(t) = i_{D1} - i_{D2} = \underbrace{2\alpha_{\mathrm{LO}}\alpha_{\mathrm{s}}\cos\varphi}_{DC} + \underbrace{2\alpha_{\mathrm{LO}}\left[\delta X_{\mathrm{s}}(t)\cos\varphi + \delta Y_{\mathrm{s}}(t)\sin\varphi\right]}_{AC} \tag{3.5}$$

Equation 3.5 indicates that this intensity difference includes a DC term proportional to the intensity of the laser source, as well as an AC term that depends on φ. Looking at the AC term in particular, it tells us that different quadratures of the signal will be measured depending on how we set φ. The amplitude quadrature is proportional to $\cos(\varphi)$

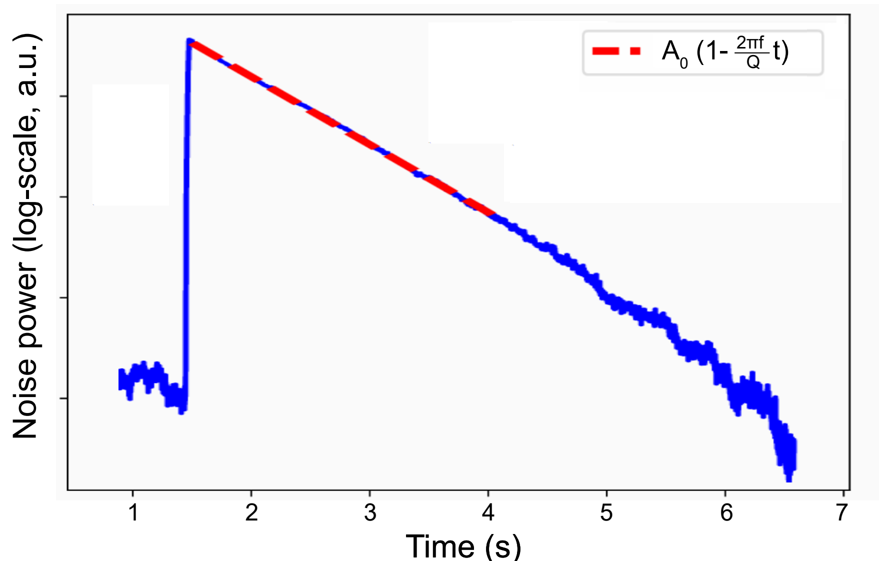

Figure 3.5: A typical result of the ringdown measurement, where the X-axis represents time, and the Y-axis shows the photodiode signal strength of the homodyne detection setup.

whereas the phase quadrature is proportional to $\sin(\varphi)$. For displacement measurement, the phase quadrature is our quadrature of interest. Therefore, φ is set to $\pi/2$, which can be achieved using a phase-locking mechanism, implemented with the help from proportional–integral–derivative (PID) controller and a phase modulator (PM) that maintain the beam phase at this specific angle. With φ locked in place, the resulting AC term is passed to the spectrum analyzer and displayed as a noise power spectrum (NPS) measurement.

3.3.2 Ringdown

Leveraging the noise power measurement provided by the homodyne detection setup, we can perform Q_{m} measurement using a technique known as the ringdown. Ringdown involves exciting the resonator of interest by driving it at its resonance frequency for a short period of time, allowing it to undergo free damped vibration after the external driver is removed (see Sec. 2.2). In this condition, the resonator's oscillation amplitude exponentially decreases over time and the noise power measurement of homodyne detection setup can be written as

$$\log(P(t)) = \log(P_0) - \frac{\Gamma t}{2} \tag{3.6}$$

where $P(t)$ is the power as a function of time, P_0 is the initial maximum power, and Γ denotes the decay rate of the resonator. By the fitting the ringdown data to Eq. 3.6, Γ can be extracted, and thus Q_{m} (see Fig. 3.5).

4

Material Characterization

As a thin film, the elastic properties of crystalline AlN vary depending on the growth condition, substrate orientation, and film thickness. Characterization of these properties is therefore a crucial first step needed to be taken before one can start with the design, simulation and fabrication of mechanical resonators from AlN thin films.

In this thesis we studied four AlN thin film samples with thickness ranging from 90 nm to 295 nm (grown by our collaborators [46]). This chapter details the characterization process of four samples on three key properties important for our nanomechanical resonator design: Young's modulus, residual stress, and intrinsic quality factor.

4.1 Young's modulus

Young's modulus, also known as the elastic modulus, is a measure of the material's stiffness. It refers to the material's ability to deform elastically when subjected to an applied force. A material with high Young's modulus will only deform slightly even under a large external force, whereas a low Young's modulus material will significantly lengthen or shorten with just a small amount of applied stress. Mathematically, the linear Young's modulus (E) is defined as

$$E = \frac{\sigma}{\epsilon}, \tag{4.1}$$

where σ is the applied stress in the linear elastic region of a given material (see Fig. 4.1), and ϵ is the induced strain.

In general, methods for evaluating Young's modulus can be grouped into two categories: static and dynamic. The static method is arguably the more commonly used approach, which typically involves applying a range of loads to the material while continuously measuring its deformation. In this thesis however, we characterize our AlN samples using the dynamic method instead due to its simplicity.

The Young's modulus characterization that we use is based on the measurement of the resonant frequencies of a cantilever-shaped structure. It has been derived analytically that the resonant frequencies of cantilever resonator (f_c) can be formulated as [30]

$$f_\mathrm{c} = \frac{\lambda_n^2}{2\pi L^2}\sqrt{\frac{Eh^2}{12\rho}}, \tag{4.2}$$

where $\lambda_1 = 1.8751$ for the fundamental mode, h is the film thickness, L is the length of

the cantilever, and ρ is the material density. A set of cantilevers with different lengths can then be used to determine the material's Young's modulus value by measuring and fitting their resonant frequencies to Eq. 4.2, given that exact dimensions of the structures and material density value are known.

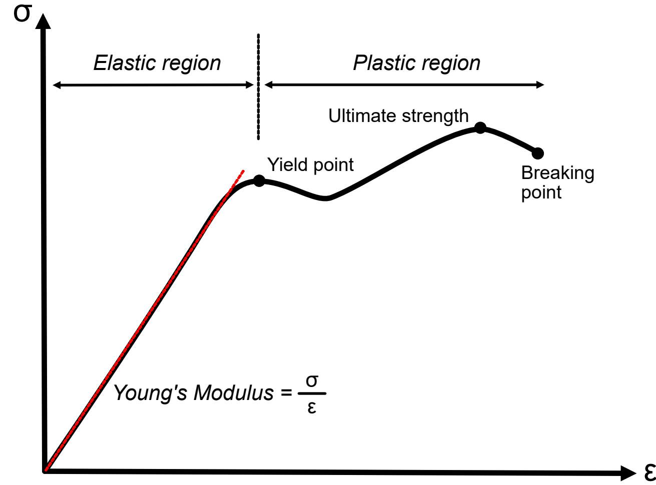

Figure 4.1: The typical shape of ductile materials' stress-strain characteristic.

Based on this concept, we fabricated cantilever-shaped resonators with lengths between 45 µm and 95 µm. We performed homodyne measurement to obtain their fundamental resonance frequency f_c. Then knowing the cantilever's dimensions and the value of AlN density (see Tab. A.1) we did the fitting and evaluated the Young's modulus of all our AlN samples. The results are presented in Fig. 4.2 and Tab. 4.1. Note that AlN 295 nm-thick samples shows lower Young's modulus compared to thinner films, which can be attributed to it being so close to the 300 nm critical thickness of crystalline AlN when grown lattice-mismatched [47].

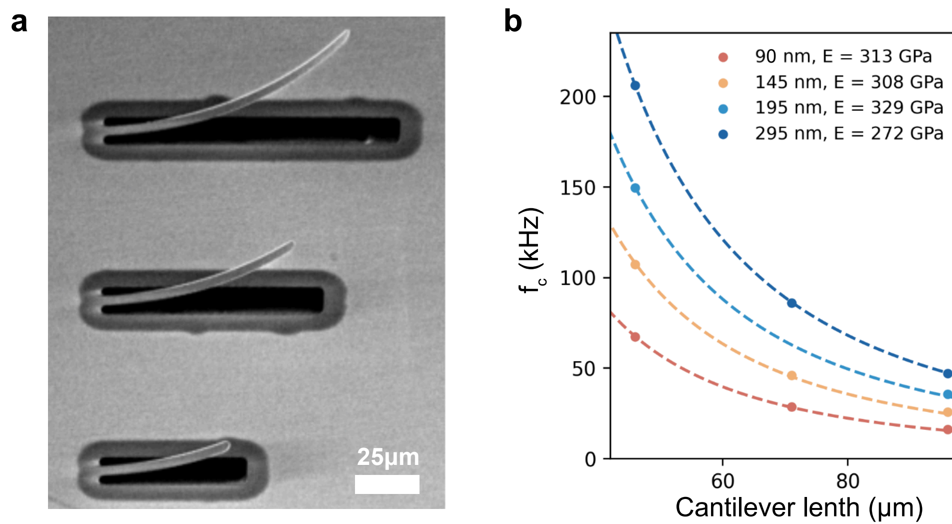

Figure 4.2: (a) Tilted SEM image of the fabricated cantilevers from 295 nm-thick AlN. (b) Mechanical frequency of the fundamental mode of the cantilevers (dots). Young's modulus is calculated from the fit (dashed line) for the different AlN film thicknesses.

h (nm)	E (GPa)
90	313
145	308
195	329
295	272

Table 4.1: Calculated Young's modulus (E) for different thickness (h) of AlN films.

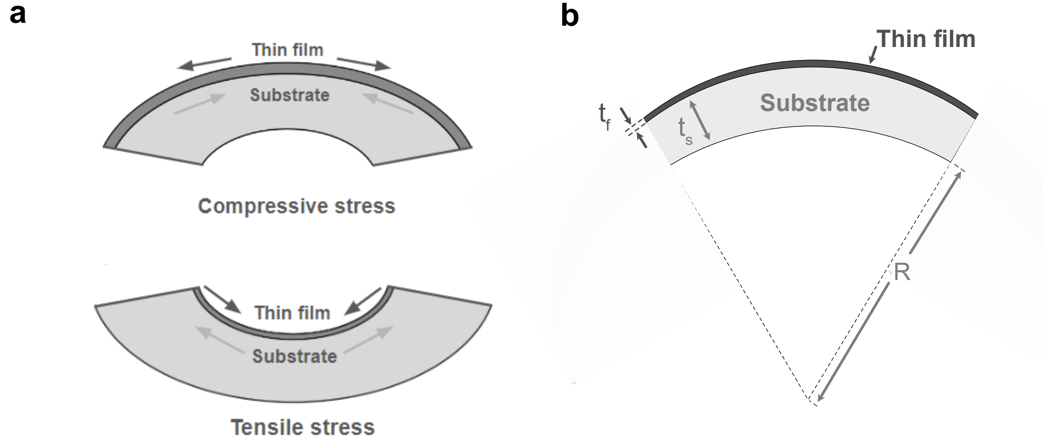

Figure 4.3: Wafer bending and film stress. (a) The shape of wafer bending for compressive and tensile stressed thin film wafers. The arrows show the directions of the expansion or contraction of both the thin film and its substrate. (b) Illustration of different components in Stoney's equation.

4.2 Residual stress

Residual stress, also called as-grown stress, is a measure of internal tension within a material, which can occur after growth of a stressed film on top of a substrate. There are two types of stress the material can undergo: compressive or tensile. In wafers containing only a single layer of thin film material deposited onto a substrate, the type of film stress is directly related to the shape of the wafer bending. As shown in Fig. 4.3a, wafers with compressively stressed thin film bend outwards whereas those with tensile-stressed thin film will bend inwards.

In addition to that, the degree of the wafer bending is linked to the magnitude of stress the film experienced. The higher the stress is, the more bending will occur. The relationship between film stress and wafer bending is well captured by Stoney's equation [48]

$$\sigma_f = \frac{E_s t_s^2}{6(1-\nu_s) t_f R}, \tag{4.3}$$

where σ_f is the stress in the thin film, E_s is Young's modulus of the substrate, t_s is thickness of the substrate, ν_s is Poisson's ratio of the substrate, t_f is thickness of the thin film, and R is radius of curvature of the substrate (see Fig. 4.3b).

In any thin film, stress is a parameter of paramount importance. Having a thin film with a particular stress can be crucial to the success or failure of the given application. For our application, we would like to have high tensile stress as it gives us three-fold benefit: increased f_{m}, Q_m, and the size of phononic bandgap. However, growing crystalline AlN with high tensile stress is challenging due to the material's tendency to develop cracks, which will be detrimental to the performance of mechanical resonators. Therefore, significant effort has been made to grow these high quality samples, obtaining residual stress as high as 1.4 GPa for 295 nm-thick AlN.

In the process of growing AlN films, residual stress has two origins: lattice mismatch and the difference in coefficients of thermal expansion (CTE) between AlN and Si. Lattice mismatch between cystalline AlN and Si (111) are 16.7 % [49], which is huge for an epitaxial grown material. Additionally, the high growth temperature of our AlN films (1100°C) further amplifies the stress as the sample cools down.

In regards to the characterization process, the most common method to characterize wafer stress typically involves measuring the wafer's bending shape. However, we could not determine the stress using this method due to the lack of necessary initial wafer parameters. Instead, we use two alternative methods to evaluate the stress in the AlN films: (i) via mechanical frequency of the AlN beam and (ii) phonon frequency shift from Raman spectroscopy. In both methods we assume a single layer of AlN film on Si substrate. In the first approach the released stress, $\sigma_{\mathrm{released}}$, is determined from the mechanical frequency of the uniform beam. In the second approach the phonon frequencies can be observed for the suspended and as-grown AlN film (that are shifted by $\sigma_{\mathrm{released}}$ and $\sigma_{\mathrm{residual}}$, respectively). However, the conversion from phonon frequency to in-plane stress is approximated with the parameters for a single-crystal case.

4.2.1 Mechanical frequency method

We can utilize a particular shape of the mechanical resonator to determine the released stress, which in this case is the form of a uniform doubly-clamped beam. The analytic formula for its fundamental resonant frequency is [30]

$$f_{\mathrm{b}} = \frac{1}{2L}\sqrt{\frac{\sigma_{\mathrm{released}}}{\rho}}. \tag{4.4}$$

As the resonant frequency is coupled to stress, measurement of the fundamental modes of beams of varied lengths can serve as a means to determine the material stress. In doing so however, one needs to pay attention to Poisson's ratio, ν, which is a measure of the material's deformation in the direction perpendicular to an externally applied force. During resonator releasing process, stress in the thin film material undergoes a stress redistribution due to not anymore attached to its substrate. The term for the stress that we measure in the suspended film is 'released-stress', $\sigma_{\mathrm{released}}$, in contrast to the initial thin film stress 'residual stress', $\sigma_{\mathrm{residual}}$. In beams, the relation between the two can be written as:

$$\sigma_{\mathrm{released}} = (1-\nu)\sigma_{\mathrm{residual}} \tag{4.5}$$

In the experiment, we fabricated doubly-clamped beams of width 2 µm and slightly curved

edge profile (see Fig. 4.4b), with varied lengths, ranging from 75 µm to 200 µm. The slightly modified edge profile was introduced to avoid cracks that our initial beam design experienced during the release process (see Fig. 4.4a).

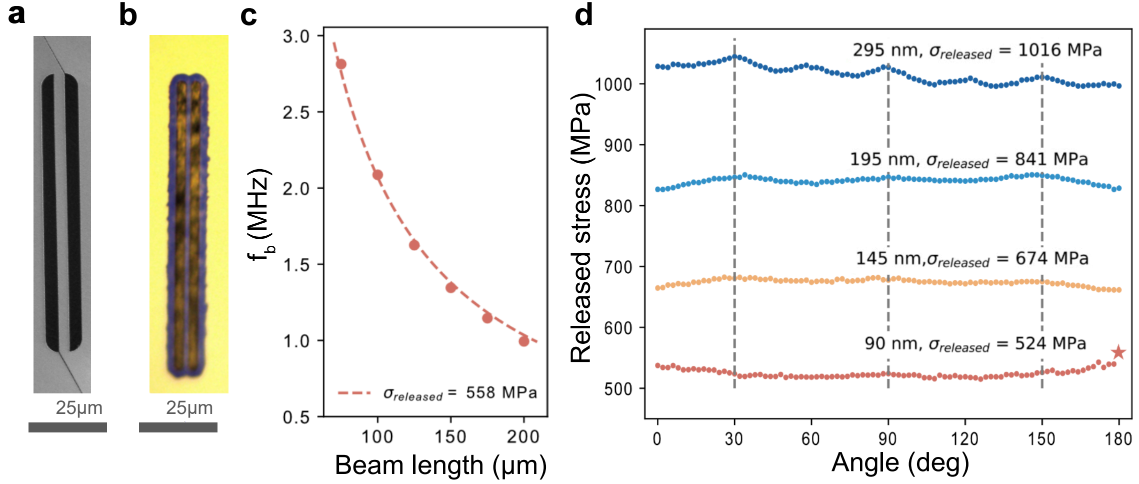

Figure 4.4: Film stress characterization via doubly-clamped beams. (a) An SEM image of a doubly-clamped beam without round edge profile experienced cracks during the release process. (b) An optical image of the revisited beam design incorporates round edge profile. (c) Released stress is calculated from the fit (dashed line). (d) Plot of AlN thin film released stress as the function of in-plane orientation with respect to the substrate.

As AlN is a crystalline material, we also varied the beams' orientation with respect to the crystalline orientation of the substrate to evaluate film stress as a function of in-plane orientation. Finally we repeated the process for all of our AlN thin film thicknesses. We performed homodyne measurements, and fitted the measured f_b to Eq. 4.4. The result is presented in Fig. 4.4d. It shows a slight orientation-dependence of the released stress with 60 degree periodicity for 195 nm and 145 nm samples, which is expected from a wurtzite-structured material due to its crystal symmetry. However, the 295 nm sample shows three extra peaks, making them appear to be 30 degree periodicity which we suspect to be caused by crystal twinning (an intergrown structure with a mirrored orientation). In addition to that, the 90 nm sample doesn't show any obvious orientation-dependence trend, which can be attributed to the minimal crystalline layer above the defect rich bottom layer [47]. All in all, the orientation-dependence is not so strong. We therefore use the average of these orientation-dependent stress to get a single value for the released stress for each AlN thickness. Finally, we used the AlN Poisson's ratio (see Tab. A.1) and Eq. 4.5, to evaluate the residual stress shown in table 4.2 below. The numbers reveal that the thicker AlN films posses higher residual stress.

h (nm)	σ_{released} (GPa)	σ_{residual} (GPa)
90	0.52	0.73
145	0.68	0.95
195	0.83	1.16
295	1.02	1.40

Table 4.2: .

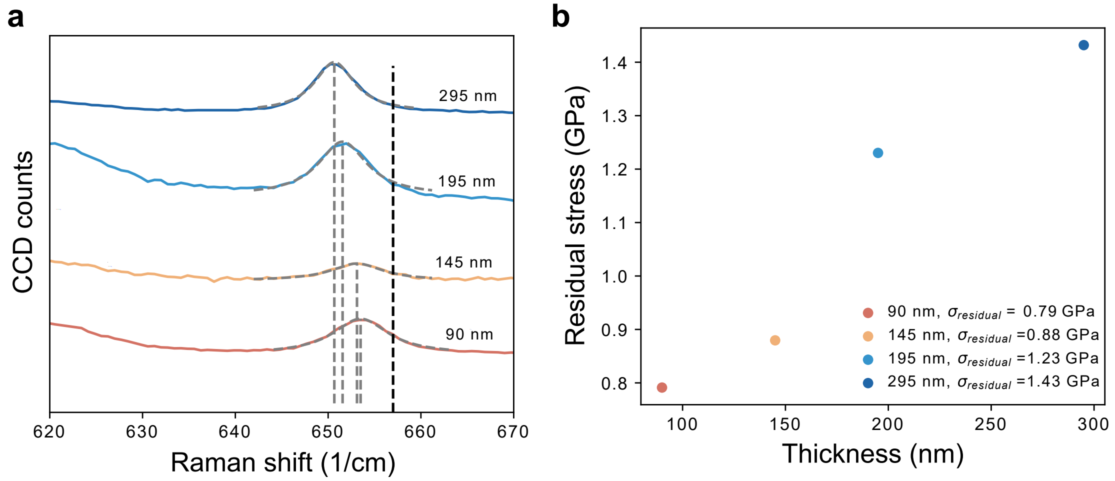

Figure 4.5: Film stress characterization via Raman spectroscopy. (a) Measured Raman spectra for different AlN film thicknesses. The black dashed lines mark the E^2 mode of an unstrained AlN film whereas the gray dashed lines are the E^2 mode for each AlN film thicknesses which is lower in energy due to the stress in the film. (b) The calculated residual stress of different AlN thicknesses.

4.2.2 Raman spectroscopy

Raman spectroscopy is a spectroscopy technique used to probe the vibrational energy modes of a sample. It is based on the phenomenon of inelastic scattering (Raman scattering) that occurrs when monochromatic light interacts with molecular vibrations, shifting the energy of the incident photons to either higher or lower energy. This energy shift provides information about the energy of the vibrational modes in the system. Stress within a material directly affects these vibration modes. Compressive stress reduces the distance between atoms, resulting in higher vibrational frequencies, whereas tensile stress increases the atomic distance, leading to lower frequencies. Due to its ability to directly probe these changes, Raman spectroscopy has been widely used in thin film stress determination.

Using our Raman microscope, we measure the Raman shift of the different AlN film thicknesses using a 532 nm laser. The measured frequency shifts (see Fig. 4.3a) were then converted into 'residual stress' values shown in Fig. 4.5b using the formula

$$\Delta\omega = 2\alpha_0\sigma_{xx}^0 \tag{4.6}$$

where $\Delta\omega$ is the Raman shift, α_0 is the proportionality constant, σ_{xx}^0 is the stress in the x-direction, and $2\alpha_0 = 4.423\,\mathrm{cm}^{-1}/\mathrm{GPa}$ [50].

The result shows the same trend obtained from the previous method, confirming that thicker AlN films have more residual stress. Moreover, the two outcomes show a good agreement with a maximum discrepancy of only 8 percent.

4.3 Intrinsic quality factor

Every material has its own intrinsic mechanic loss mechanisms and a figure of merit is an intrinsic quality factor. It is therefore required to determine for a new material this value of Q_{int}. To determine the intrinsic quality factor of our AlN thin film, we use the concept of generalized dissipation dilution of double-clamp beams described in Sec. 2.2.2.

Using the same beams from the stress characterization, we measured each individual beam's quality factor and plotted their values as a function of beam orientation (see Fig. 4.5a). Due to the not so strong orientation-dependent stress attained in the previous section, we average their values and plot them as a function of length and film thickness (see Fig. 4.5b). The intrinsic quality factor, Q_{int}, can then be fitted from the data using equation 2.13 and 2.15. The results shown in Tab. 4.3 suggest that 195 nm thick AlN possesses the highest Q_{int}.

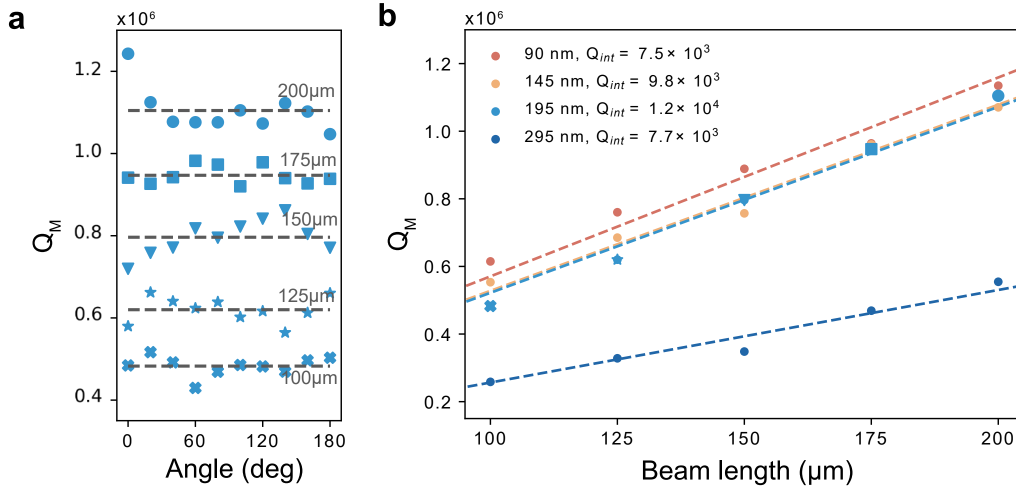

Figure 4.6: Intrinsic quality factor characterization. (a) Quality factor of beams of different lengths as a function of beam orientation for 195 nm thick AlN. (b) Quality factors of beams of different lengths and thickness. Intrinsic quality factor is calculated from the fit (dashed line) for the different AlN film thicknesses.

h (nm)	$\epsilon_{\text{released}}$ (%)	Q_{int}
90	0.17	7.5×10^3
145	0.22	9.8×10^3
195	0.25	1.23×10^4
295	0.38	7.7×10^3

Table 4.3: Evaluation of released strain ($\epsilon_{\text{released}}$) and intrinsic quality factor (Q_{int}) as a function of AlN film thickness (h).

4.4 Summary

Tab. 4.4 shows the compiled results obtained throughout this chapter. Note that here we report our final σ_{residual} using the average values of the σ_{residual} acquired from the mechanical frequency method and Raman spectroscopy.

h (nm)	E (GPa)	σ_{residual} (GPa)	$\epsilon_{\text{released}}$ (%)	Q_{int}
90	313	0.76	0.17	7.5×10^3
145	308	0.91	0.22	9.8×10^3
195	329	1.19	0.25	1.23×10^4
295	272	1.41	0.38	7.7×10^3

Table 4.4: Summary of elastic properties of different thicknesses of AlN film: Young's modulus, residual stress, and intrinsic quality factor.

5

Results

This chapter deals with the results from the design, fabrication, and characterization of three types of phononic-shielded nanomechanical resonators realized in tensile-strained AlN. We present the results in such a way that allows a direct performance comparison between different designs at each development step.

5.1 Design

5.1.1 PnC unit cell bandgap simulation

Working with a crystalline material, we select the PnC unit cell patterns that preserve the inherent wurtzite crystal symmetry of crystalline AlN to avoid unwanted stress discrepancy between areas within them. We investigated three different PnC patterns: honeycomb, snowflake, and dandelion.

The honeycomb PnC pattern [15] (Fig. 5.1a) consists of periodic circular holes arranged in a honeycomb-like pattern with only two crystal parameters: lattice constant a and hole radius r. Although widely featured in numerous studies, to the best of our knowledge, the honeycomb PnC has not been realized in any tensile-stressed crystalline material so far.

The snowflake PnC pattern [51] (Fig. 5.1b) is characterized by repeating snowflake-like holes arranged in a hexagonal lattice. It has three parameters: lattice constant a and leg width w_1, and leg separation distance w_2. In addition to that, we introduced an additional variable, fillet radius r_f that we fixed at $2\,\mu\text{m}$ to mitigate the formation of cracks as discussed in Sec. 4.2.1.

Finally, the dandelion PnC pattern [52] (Fig. 5.1c) is a close resemblance of the honeycomb PnC pattern, except that it features rounded triangle-shaped holes instead of circular ones. The pattern is defined by three parameters: lattice constant a and tether width w_1, and fillet radius r_f. Unlike the snowflake PnC pattern, the fillet radius r_f in this pattern serves as a strong parameter for driving the formation of a phononic bandgap.

As discussed in section 3.1, the engineering of the PnC starts with the analysis of the band diagram in ω-$\vec{k}$ space. As our unit cells are in the shape of a rectangular, the high-symmetry points Γ-X-M were used to define their Brillouin zone. The band diagrams are then obtained via Comsol as following:

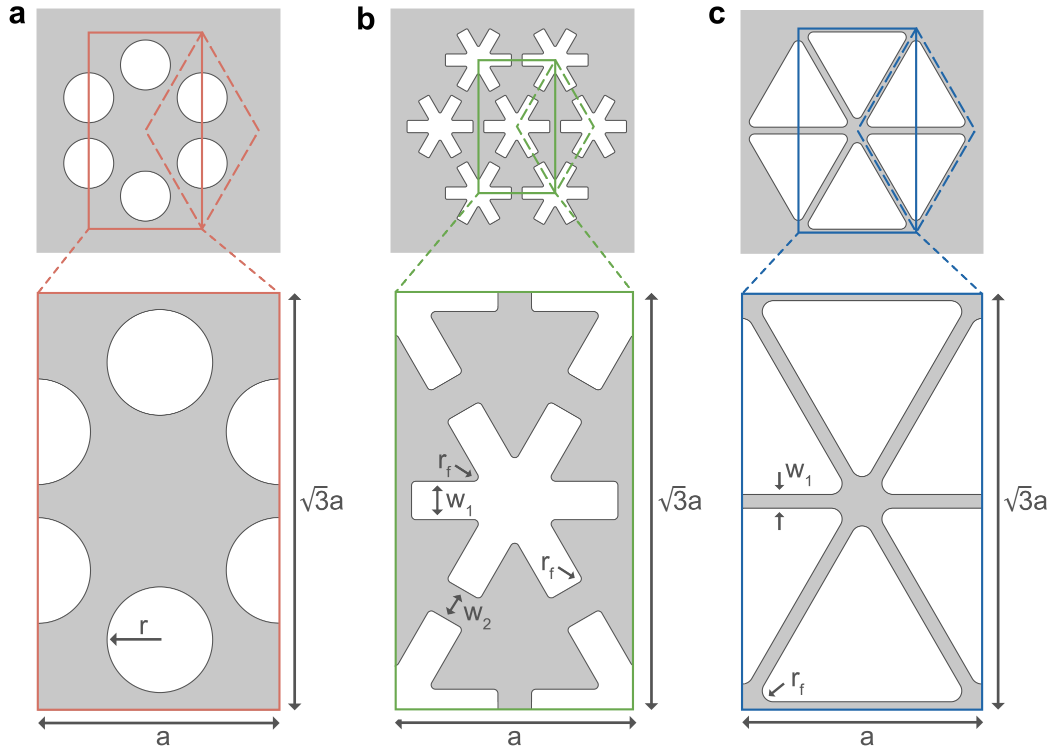

Figure 5.1: The three different PnC patterns. (a) Honeycomb, characterized by circular holes with radius r, arranged in a honeycomb-like pattern. (b) Snowflake, featuring snowflake-shaped voids in a hexagonal lattice with varying leg widths w_1 and leg separation w_2. Additional fillet radius r_f is introduced to avoid edge-cracks during the fabrication process. (c) Dandelion, described by a hexagonal grid of rounded triangular cuts with central openings defined by tether widths w_1 and fillet radius r_f. Lattice constant parameter for all the patterns are denoted by a.

PnC	a (µm)	r (µm)	r_f (µm)	w_1 (µm)	w_2 (µm)
Honeycomb	110	0.245a	-	-	-
Snowflake	110	-	2	15.4	17.6
Dandelion	110	-	5	6.35	-

Table 5.1: Crystal parameters used in FEM simulations of the fabricated PnC patterns. The lattice constants are fixed at 110 µm to ensure similar center frequencies of the bandgaps across all three PnC designs.

1. set the PnC parameters (r, a, w_1, w_2),
2. define the boundary condition (Floquet periodicity[1]),
3. simulate the dispersion relation for the chosen k-vector directions.

Simulation results in Fig 5.2 show the band diagram obtained via Comsol simulation for each pattern using particular crystal parameters detailed in Tab. 5.1. Note that each diagram features a colored region that highlights the frequency range where phononic bandgaps are present. Yet, they are not complete gaps as there are still modes that cross

[1] A boundary condition that treats object of interest as an infinitely repeating structure in space [53]

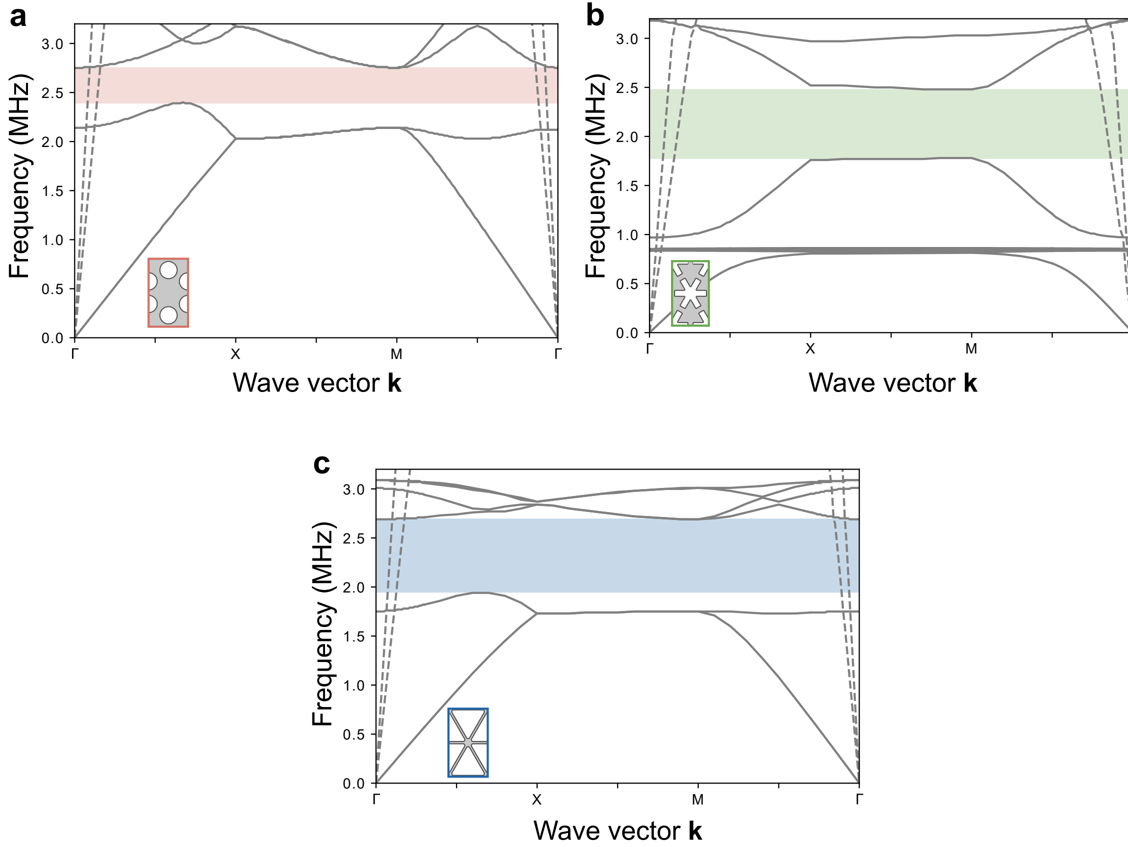

Figure 5.2: Band diagram of the fabricated PnC patterns. (a) Honeycomb, (b) snowflake, (c) dandelion. Out-of-plane modes are denoted with solid lines whereas in-plane modes are denoted with dashed lines. The relative bandgap for honeycomb, snowflake, and dandelion PnC pattern are 0.14, 0.33, and 0.32 respectively.

near the Γ point. They are therefore referred to as quasi-bandgaps which suppress only the out-of-plane modes. Fortunately, these out-of-plane modes are precisely the ones we are focused on in this work, making this quasi-bandgap function perfectly for our application.

When analyzing multiple band diagrams, the *relative bandgap* is a commonly used metric for comparing bandgaps across different diagrams. This metric offers a more universal way to describe bandgaps by normalizing the bandgap size relative to the central frequency of the gap, which can be expressed as:

$$relative\ bandgap = \frac{f_{\text{top}} - f_{\text{bottom}}}{f_{\text{center}}} \tag{5.1}$$

where f_{top} is the upper frequency limit of the bandgap, f_{bottom} is the lower frequency limit of the bandgap, f_{center} is the central frequency of the bandgap, calculated as $\frac{f_{\text{top}}+f_{\text{bottom}}}{2}$. Using this metric, the relative bandgap for honeycomb, snowflake, and dandelion band diagram particularly shown in Fig 5.2 are 0.14, 0.33, and 0.32 respectively.

Going further, Fig. 5.3 presents the results of a systematic study on how the bandgap varies

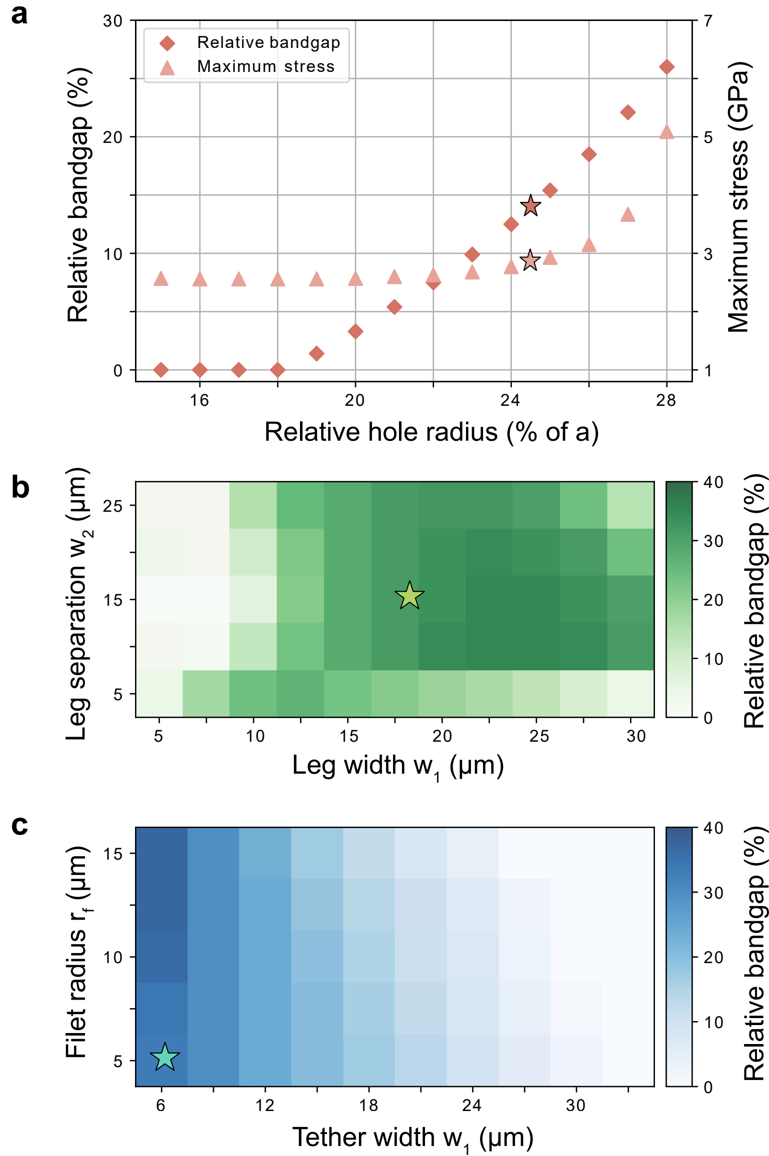

Figure 5.3: Relative bandgap of the three PnC patterns as a function of their crystal parameters. (a) Honeycomb, (b) snowflake, and (c) dandelion.

with different crystal parameters. The lattice constants were fixed at 110 µm to ensure similar center frequencies of the bandgaps across all three PnC designs. In Fig 5.3a, the honeycomb PnC pattern shows no bandgap for hole radius below $0.18a$, a growing bandgap size between $0.18a$ and $0.28a$. The value $0.285a$ represents the maximum hole radius, beyond which two adjacent circles begin to overlap. Throughout these range however, increasing the bandgap comes with the trade-off of higher film maximum stress. Due to fabrication constraints that will be discussed in the following section, we chose to limit the stress of our design to 3 GPa. Based on this requirement, a hole radius of $0.245a$ was selected.

In the snowflake PnC (Fig. 5.3b), the 2D map displays the relationship between the relative bandgap with both w_1 and w_2. The plot reveals that the widest bandgap is at points with a specific combination of w_1 and w_2. The PnC parameters chosen for the snowflake PnC,

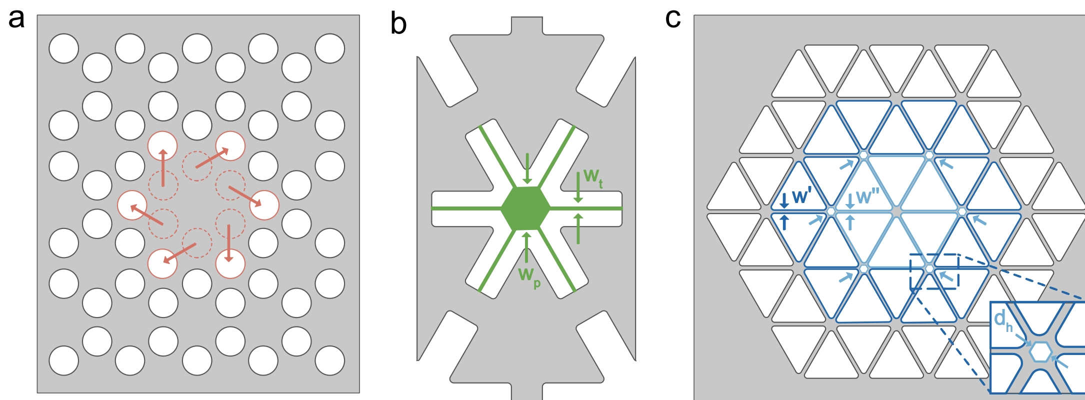

Figure 5.4: Defect geometry for each PnC pattern (a) the defect in the honeycomb PnC pattern is made by fusing several unit cells and shift holes in the center outwards. (b) Defect in snowflake PnC pattern comes in the form of hexagonal trampoline, introduced in the middle of a snowflake void, described by tether width w_t and the width of the pad w_p. (c) The dandelion defect is made by combining several unit cells and modifying the tether widths w' and w'' of highlighted unit cells as well as introducing six hexagonal holes d_h.

as shown in Table 5.1, are close to this optimal point.

A simpler relation can be observed in the plot for the dandelion PnC pattern (Fig. 5.3c). Here, the bandgap increases with the reduction of w_1 and the increase in r. For fabrication purposes however, we choose to limit r_f to 5 µm, as a larger radius would result in a bigger pad and longer etching time.

5.1.2 PnC defect engineering

While simulating the bandgap of a PnC pattern is a straightforward process, designing a defect with a specific frequency and mode shape is more complex as a high degree of flexibility is inherent to the process. Nevertheless, the commonly used strategy is to take the PnC unit cell as a base template and modify it so that one or more of its resonance frequencies shift into the bandgap. An example of this approach is the defect in a honeycomb PnC pattern shown in Fig. 5.4a which is formed by combining several unit cells and shifting the central hole outward, resulting in a large central pad with highly tapered tethers at the edges.

Another example is the defect of the dandelion PnC pattern (Fig. 5.4c), created by combining multiple unit cells together and introducing three changes: taper the tether widths w' and w'' to $1/\sqrt{2}$ and $1/\sqrt{3}$ of that of w_1 respectively, and introduce six hexagonal holes d_h at six pads around the central area. These modifications result in 1) an increase in the stress of the tethers 2) a reduction in motional mass, and 3) a shortening of the center pad tethers. Together, these changes shift the mechanical resonance frequency of the central pad into the bandgap.

Conversely, the snowflake defect was created differently (Fig. 5.4b). In this case, the defect takes the form of a hexagonal trampoline introduced into the empty area at the center of

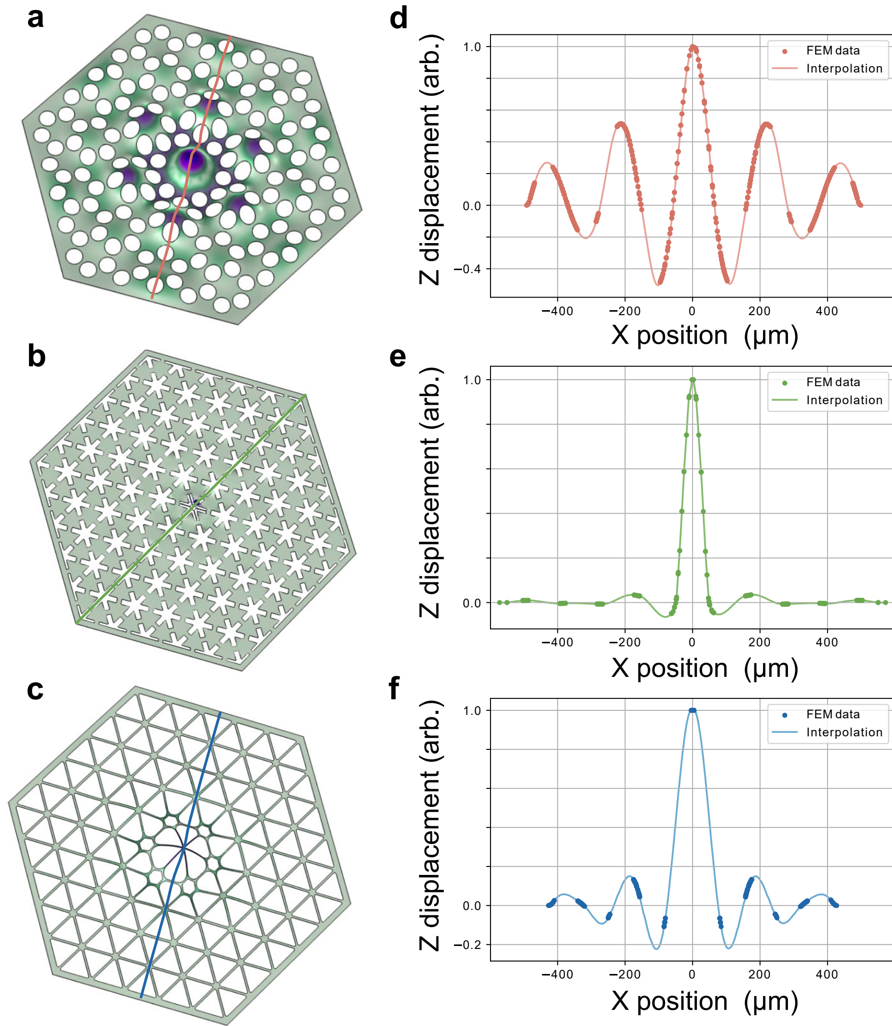

Figure 5.5: The complete structures of the three PnC patterns and the displacements of their corresponding defect modes. (a,d) Honeycomb, (b,e), snowflake, and (c,f) dandelion.

the structure, described by tether width w_t and the width of the pad w_p.

5.1.3 Membrane assembly

With both PnC patterns and their defects have been defined, the complete membrane structures can then be constructed. This is done by placing the defect design in the middle and layering several units of PnC unit cells around it, resulting in the full structures shown in Fig. 5.5a-c.

In a well designed phononic shield the defect exhibits its resonance frequency inside the bandgap. Then, the isolation of the defect mode from its clamping boundaries can be seen as an exponential decay of its out-of-plane displacement towards the edge of the resonator. Shown in Fig. 5.5d-f are the displacement profiles of the localized modes, the hallmark of soft-clamping.

5.1.4 Evaluation and optimization of mechanical quality factor

As explained in Sec. 2.2, the evaluation of Q_{m} requires the values of both Q_{D}, and Q_{rad}. To acquire these values, we conducted an eigenfrequency study in COMSOL on all three PnC patterns. Additionally, the analysis was performed as a function of the number of unit cells, providing a comprehensive view of how Q_D, and Q_{rad} vary with changes in the number of unit cells.

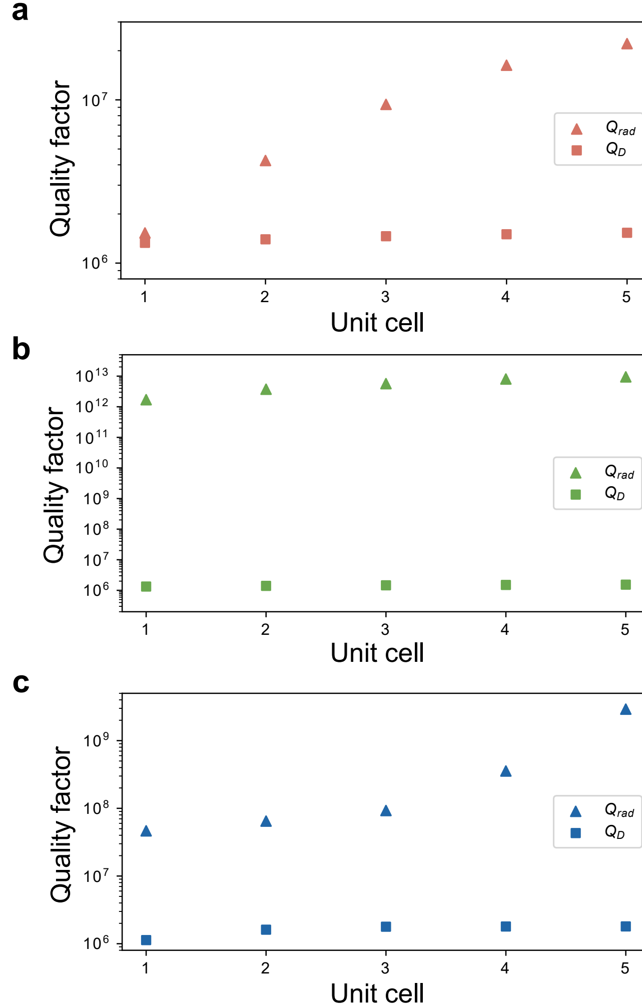

Figure 5.6: Diluted internal quality factor Q_{D} and radiative quality factor Q_{rad} as a function of the number of PnC unit cells for all three PnC patterns (a) Honeycomb, (b) snowflake, and (c) dandelion.

The simulation results in Fig. 5.6 indicate that Q_{rad} increases with the number of PnC unit cells for all three PnC patterns, while Q_{D} remains relatively constant. This increase in Q_{rad} is expected, as a higher number of unit cells provides better suppression of phonon radiation toward the support. Given that Q_{rad} already exceeds Q_{D} by more than an order of magnitude in all patterns we chose to focus the rest of optimization process to three PnC unit cells.

5.1.4.1 Defect optimization

As shown in Fig. 5.4, several free parameters were used to define the defect in both snowflake and dandelion PnC patterns. As the design of the defect significantly impacts its Q_m values, defect optimization is therefore needed to make sure that we obtain the highest Q_m possible.

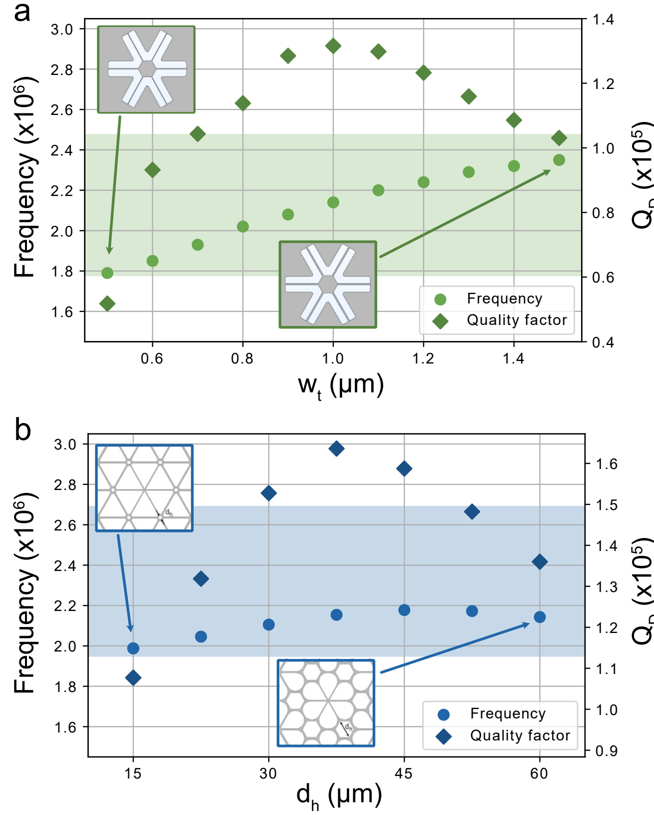

Figure 5.7: Optimization of defect design for snowflake and dandelion PnC patterns. (a) For the snowflake PnC pattern, the resonance frequency and Q_D are plotted as a function of w_t, with w_p fixed at 20 µm. The plot shows that Q_D reaches its peak when the resonance frequency is closest to the central bandgap frequency. (b) For the dandelion PnC pattern, the resonance frequency and Q_D are plotted as a function of d_h. An optimal hole size can be observed where the Q_D enhancement from the increase of stress and the reduction of bending are maximized.

For the snowflake PnC pattern, the optimization was performed by varying w_t, with w_p fixed at 20 µm. The result (see Fig. 5.7a) indicates an optimal hole size that yields the highest Q_D, occured when the resonance frequency is closest to the center of the bandgap. This aligns with expectations, as the performance of the bandgap is determined by the proximity of the defect's resonance frequency to the nearest mode outside the bandgap. If the resonance is not centered, the distance to these modes becomes smaller, reducing the effectiveness of the PnC shielding.

For the dandelion PnC pattern, the optimization is carried out by evaluating Q_m for different hexagonal hole radii d_h, yielding Fig. 5.7b. We observe that changes in d_h affect both Q_D and frequency. Not as simple as in the snowflake case however, Q_D in this PnC

pattern doesn't only depend on the proximity of its resonance frequency to the center frequency of the bandgap, but also the distribution of stress and bending within the defect area. Thus, the peak Q_{D} reflects the value of d_h that maximizes the impact from those three factors.

5.1.4.2 Thickness dependence

As predicted by the dissipation dilution formula (see Sec. 2.2.2), film thickness plays a major role in determining the achievable Q_{m}. We therefore performed the simulation utilizing the AlN material parameters acquired from the previous chapter. Table 5.2 presents the simulation results for the different PnC patterns for various AlN thicknesses.

As the thickness decreases, several trends can be observed:

1. As the stress decreases, the resonance frequencies also decrease with thinner AlN films.

2. Q_{m} generally increases for thinner AlN films, although the exact value depends also on both stress and Q_{int}, as indicated by the simulation result for 145nm AlN.

All in all, the best results for both Q_{m} and $Q_{\mathrm{m}} \times f_{\mathrm{m}}$ for all three PnC patterns are obtained with 90nm AlN.

h [nm]	PnC	Bandgap [MHz]	f_{m} [MHz]	Q_{m}	$Q_{\mathrm{m}} \times f_{\mathrm{m}}$ [Hz]
90	HC	1.75 - 2.05	1.8	6.5×10^6	1.2×10^{13}
	SF	1.47 - 2.04	1.62	4.6×10^5	7.4×10^{11}
	Dan	1.41 - 1.97	1.63	6.7×10^6	1.1×10^{13}
145	HC	1.91 - 2.20	1.96	4.1×10^6	8.1×10^{12}
	SF	1.44 - 1.84	1.70	1.8×10^5	3.2×10^{11}
	Dan	1.52 - 2.15	1.72	4.1×10^6	7.2×10^{12}
195	HC	2.19 - 2.52	2.25	3.6×10^6	8.0×10^{12}
	SF	1.57 - 2.11	1.95	2.4×10^5	4.6×10^{11}
	Dan	1.77 - 2.46	2.04	4.0×10^6	8.3×10^{12}
295	HC	2.33 - 2.75	2.45	1.4×10^6	3.5×10^{12}
	SF	1.77 - 2.45	2.14	1.3×10^5	2.8×10^{11}
	Dan	1.93 - 2.68	2.1	1.5×10^6	3.2×10^{12}

Table 5.2: Simulated results of f_{m}, Q_{m}, and $Q_{\mathrm{m}} \times f_{\mathrm{m}}$ for different AlN thickness.

5.2 Fabrication

5.2.1 Honeycomb PnC

The Honeycomb PnC was the first design we attempted to fabricate using a 295 nm-thick AlN film. Despite having a working process flow for fabricating other nanomechanical resonator designs in AlN films, the honeycomb samples consistently failed to be released during the XeF_2 etch release process (see Fig. 5.8). Numerous efforts were made to identify the root cause of this issue, including attempts to reduce the maximum stress in the

structure below 2.5 GPa, a stress level that had been achieved in successfully fabricated devices, according to our simulation result.

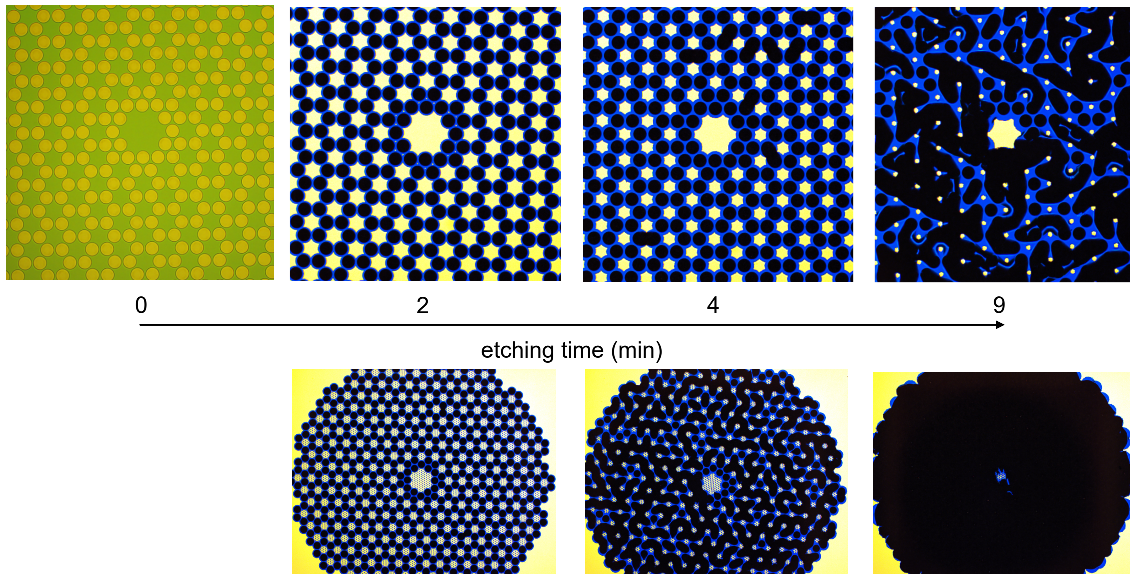

Figure 5.8: Optical images of Honeycomb at different etching times. Top panel: without additional etching holes, bottom panel with additional etching holes on the pads.

Due to limited time and wafer availability however, we eventually decided to discontinue the fabrication attempts for the honeycomb design and focus on other PnC patterns. As a result, no honeycomb devices have been successfully fabricated.

A plausible explanation comes from a simulation of the release process dynamics. Simulation results suggest that the isotropic release of XeF_2 could create sharp edges in the etched substrate beneath the structure, resulting in locally stressed points that can reach a stress as high as 10 GPa (see Fig. 5.9). This excessive stress likely causes the structure to fail. Based on this finding, it might then be possible to realize this device by using an anisotropic release process instead of an isotropic one to avoid the formation of these high-stress edges.

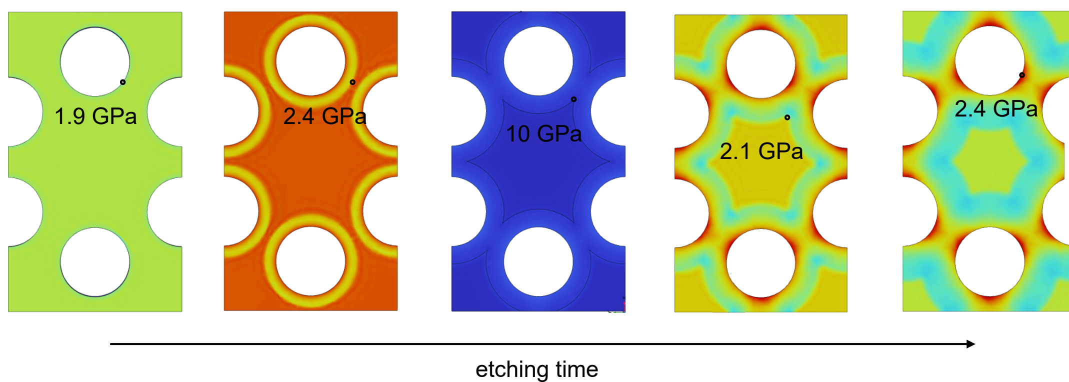

Figure 5.9: Simulation of the release process. FEM simulation indicating the maximum stress of the structure during the release process.

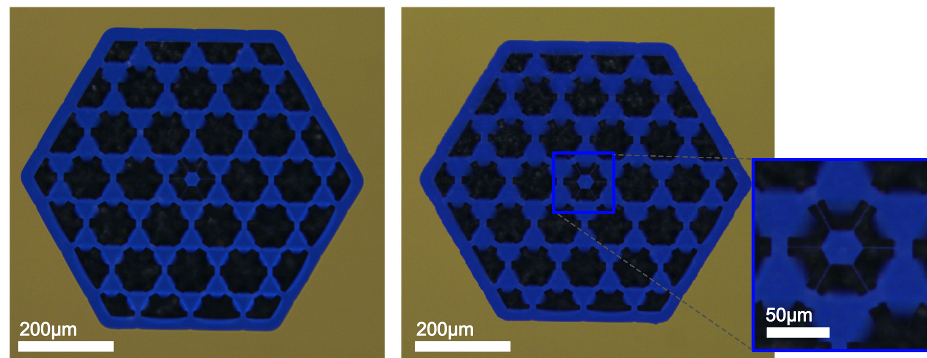

Figure 5.10: Optical images of two successfully fabricated snowflake PnC devices on 295 nm-thick AlN films

5.2.2 Snowflakes

The snowflake PnC pattern was the second design we attempted to fabricate, also using the 295 nm-thick AlN films. In contrast to the challenges faced with the honeycomb devices, the fabrication process for the snowflake chips proceeded smoothly, including the previous problematic XeF_2 etch release. As a result, two functional devices were successfully fabricated. Our hypothesis for this successful fabrication is that the flexible tips of the snowflake pattern act as a stress-relief mechanism, preventing stress from accumulating within the structure during the release process. One notable point from the optical images of the successfully fabricated devices (see Fig. 5.10) is that the tips of the snowflake pattern sagged downwards, contrary to our initial expectation that they would buckle upwards.

5.2.3 Dandelion

We successfully realized dandelion devices using 295 nm and 90 nm films, resulting in several fully functional devices. Optical and SEM images of one of these devices can be seen in Fig. 5.11.

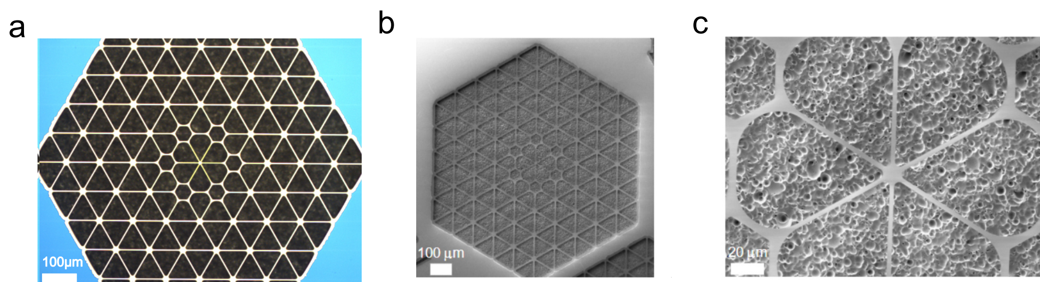

Figure 5.11: Optical and SEM images of fabricated Dandelion PnC devices. (a) Optical image of a fully fabricated Dandelion device, showing the hexagonal lattice structure with a well-defined central defect.(b) SEM image of the entire Dandelion PnC device. (c) Zoomed-in SEM image of the center defect area.

5.3 Characterization

5.3.1 Snowflake

Characterization of Q_m and resonance frequency of the snowflake devices were performed on the successfully fabricated samples. Fig. 5.12 presents the experimental results alongside COMSOL simulation results for validation.

The top plot shows the noise power spectrum (NPS), where resonance peaks are observed across a frequency range of 0.2 to 2.5 MHz. There, the strong peaks correspond to the device's mechanical resonances whereas the background levels between the peaks represent the noise floor of the measurements. In the lower plot, Q_m is plotted against the resonance frequency. The open circles represent FEM simulation data, and the solid markers show the measured results from two snowflake devices. The open and solid starts represent the simulated and suspected localized mode. Overall, the experimental and simulation

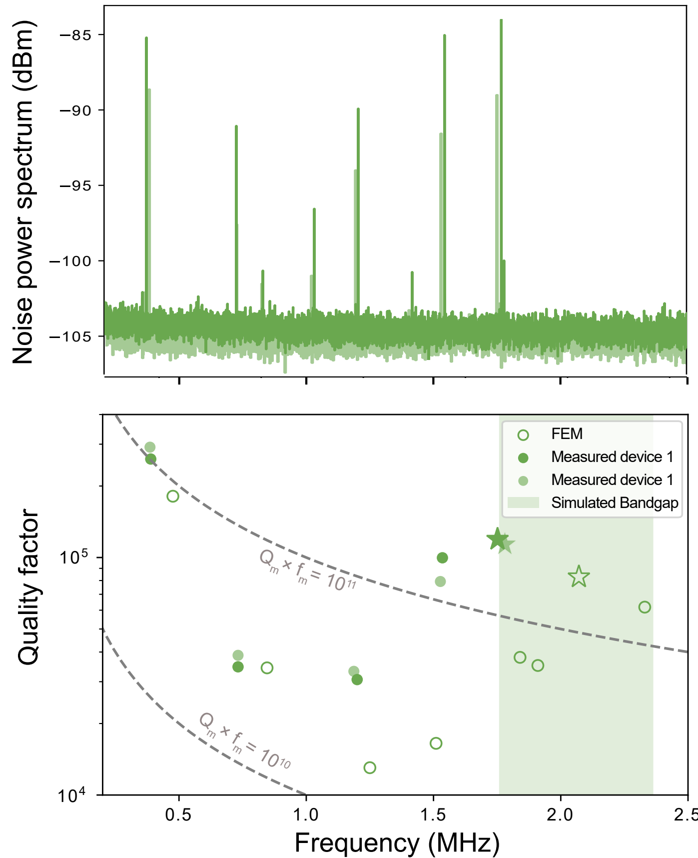

Figure 5.12: Snowflake characterization result. The top plot shows the noise power spectrum, highlighting resonance peaks between 0.2 and 2.5 MHz, corresponding to the mechanical resonances of the device. The lower plot compares the Q_m as a function of resonance frequency for both measured data (solid markers) and COMSOL simulation results (open circles). The open and solid stars represent the simulated and suspected localized mode. The shaded green region represents the frequency range in which the bandgap is to be expected.

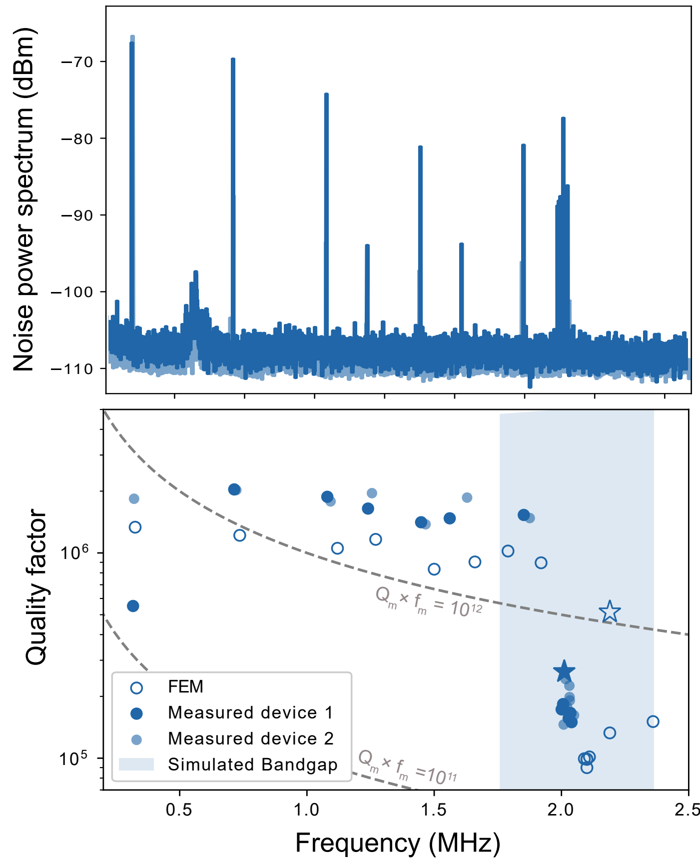

Figure 5.13: Characterization of the 295 nm dandelion PnC devices. The top plot shows the noise power spectrum, highlighting resonance peaks between 0.2 and 2.5 MHz, corresponding to the mechanical resonances of the device. The lower plot compares the Q_m as a function of resonance frequency for both measured data (solid markers) and COMSOL simulation results (open circles). The open and solid stars represent the simulated and suspected localized mode. The shaded blue region represents the frequency range in which the bandgap is to be expected.

data show good agreement. However, the frequency discrepancies between the FEM and measured results suggest the presence of stress differences between the fabricated devices and the simulated model.

5.3.2 Dandelion

Characterization of dandelion devices was carried out on several fabricated samples.

As before, Fig. 5.13 presents both the NPS and the experimental Q_m values, along with the simulation results for the 295 nm dandelion devices. From the figure, we can observe the following key points:

1. Several modes densly measured around 2 MHz are most likely to be edge modes, present due to the relatively wide under-etched edges.

2. One of these modes shows significantly higher power, indicating that it could be the

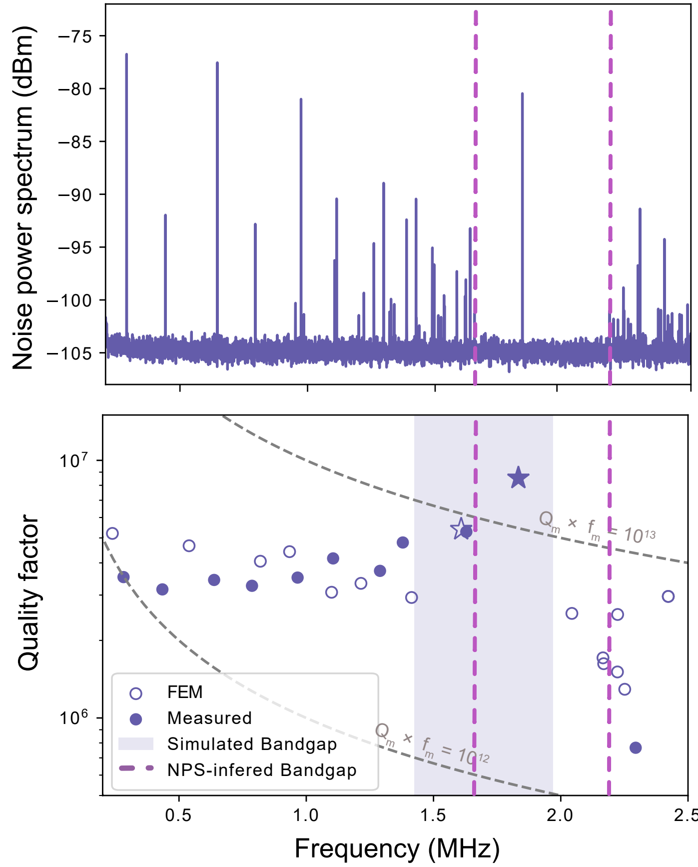

Figure 5.14: Characterization of the 90 nm dandelion PnC devices. The top plot shows the noise power spectrum, highlighting resonance peaks between 0.2 and 2.5 MHz, corresponding to the mechanical resonances of the device. The lower plot compares the Q_m as a function of resonance frequency for both measured data (solid markers) and COMSOL simulation results (open circles). The open and solid stars represent the simulated and suspected localized mode. The shaded greyish purple region represents the frequency range in which the bandgap is to be expected from the simulation, whereas the area between the two purple lines represents the frequency range in which the bandgap is suggested from the NPS data.

defect mode.

3. COMSOL simulations suggest that the mediocre Q_m values of the defect modes can be attributed to the presence of these nearby edge modes.

For the 90 nm devices, a total of four functional devices were fabricated. Characterization was performed on all of them, and an overview of the measured Q_m values for the defect modes is shown in Fig. 5.15.

Fig. 5.14 provides a detailed view of the NPS and all the measured Q_m values of our best device. From this data, we can observe the following:

1. The presence of a defect mode is convincing as the NPS plot shows a clear separation

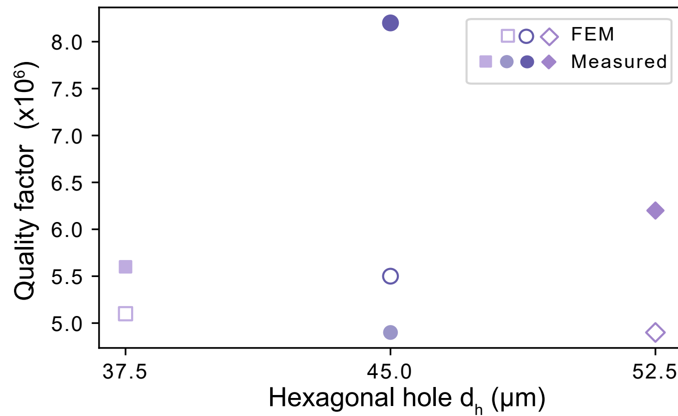

Figure 5.15: Q_m of defect modes of 90 nm dandelion devices as a function of hexagonal hole diameter d_h. The plot compares FEM simulation results (open markers) with experimentally measured Q_m values (filled markers)

between it and other modes outside the bandgap.

2. The defect mode reaches Q_m as high as 8 million at 1.8 MHz, resulting in a $Q_\mathrm{m} \times f_\mathrm{m}$ product of 1.5×10^{13}.

3. The evidence for soft clamping is strong as Q_m of the defect mode is upto a factor of two higher than of other modes.

5.4 Conclusion

Fig. 5.16 presents the compiled results obtained throughout this chapter, showing a good agreement between the simulation and experimental data. These results indicate that the simulation method employed in this thesis effectively captures the underlying physics of real devices. While the honeycomb device could not be successfully fabricated, the simulations offer valuable insights and strong guidance for future work and further optimization.

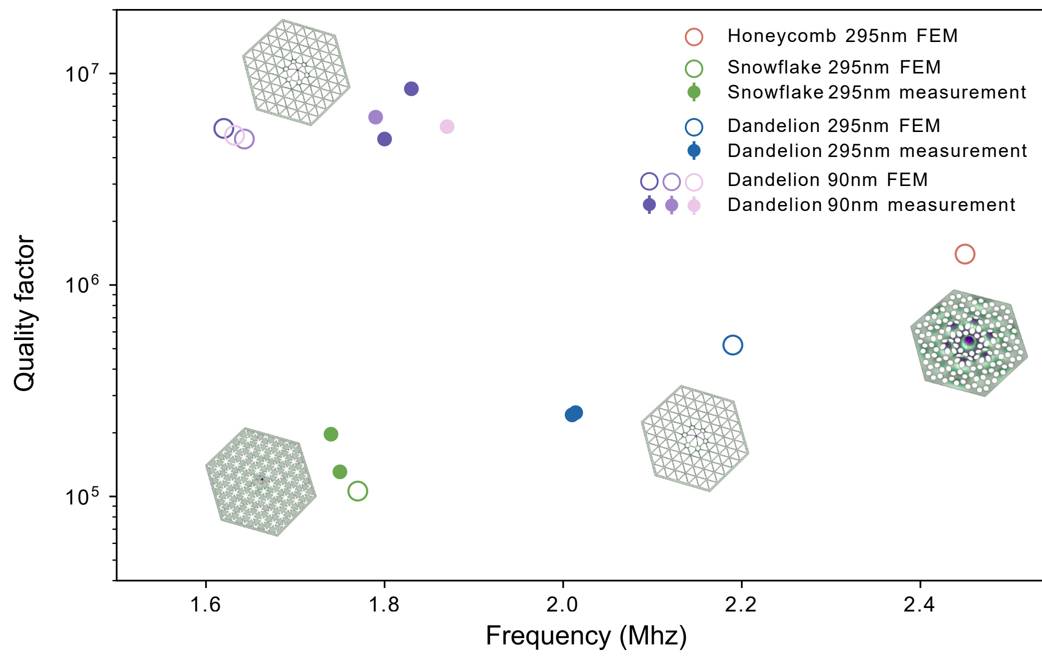

Figure 5.16: Summary of simulation and experimental results for all three PnC designs.

6

Conclusion and Outlook

The main objective of this thesis was to develop phononically-shielded, high-Q nanomechanical resonators from crystalline aluminum nitride thin films. Indeed, we have successfully accomplished this goal by realizing multiple of these devices on 90 nm thick high-stress AlN films. Our best device demonstrates Q_m of 8.6×10^6 and $Q_\mathrm{m} \times f_\mathrm{m}$ product as high as 1.5×10^{13}, formally placing it within the quantum regime at room temperature

Alongside that core task, we also carried out comprehensive characterizations of four AlN films with thicknesses ranging from 90 nm to 295 nm. This included the evaluation of their elastic properties, such as Young's modulus, residual stress, and intrinsic quality factor. With remarkably high Q_int and stress, we showed that AlN is indeed a promising material to challenge the domination of SiN in the field of nanomechanics.

We have gained profound insights, some of which are:

- Soft clamping has proven to be a versatile tool in the development of high-Q nanomechanical resonators. By providing isolation both spectrally and spatially, it effectively avoids the issue of phonon tunneling losses in these resonators.

- Dissipation dilution has proven to be a powerful framework for Q_m optimization, as it effectively captures and quantifies bending losses which are arguably the most prominent loss mechanism in most nanomechanical resonator designs.

Future work can explore reducing the thickness of the AlN films as the ever higher Q-factor can be expected. There is of course the caveat that the residual stress decreases with thinner AlN films, in contrast to SiN which can maintain a residual stress of 1 GPa even at thicknesses as low as 20 nm.

In related work, we found that the AlN thin films first have an about 70 nm-thick defect-rich layer [47]. We suspect that the presence of this defect layer contributes to the reduction in total stress within the film. Consequently, we aim to explore methods to grow AlN films without this defect layer at the interface, as its elimination could improve the overall film quality and stress retention.

The intriguing next step would be to exploit the piezoelectric properties of AlN. A straightforward approach to achieve this would involve growing an electrode layer beneath and above the AlN film, enabling easy access to the piezoelectric functionality.

All in all, aluminum nitride is already a well-established material in the standard semiconductor industry. By integrating a direct piezoelectric control, we aim to further explore and realize AlN full potential as nano-electromechanical resonator for emerging quantum applicatons.

Bibliography

[1] S. Schmid, L. G. Villanueva, and M. L. Roukes, *Fundamentals of nanomechanical resonators*, vol. 49. Springer.

[2] R. Kubo, "The fluctuation-dissipation theorem," *Reports on Progress in Physics*, vol. 29, p. 255–284, Jan. 1966.

[3] F. Hoffman, "An introduction to fourier theory," *Extraído el*, vol. 2, 1997.

[4] A. A. Shabana, *Theory of vibration*, vol. 2. Springer, 1991.

[5] D. M. Stefanescu, *Handbook of force transducers: principles and components*. Springer Science & Business Media, 2011.

[6] A. Eichler, "Ultra-high-q nanomechanical resonators for force sensing," *Materials for Quantum Technology*, vol. 2, p. 043001, Dec. 2022.

[7] V. M. Mecea, "From quartz crystal microbalance to fundamental principles of mass measurements," *Analytical Letters*, vol. 38, p. 753–767, Mar. 2005.

[8] J. Chaste, A. Eichler, J. Moser, G. Ceballos, R. Rurali, and A. Bachtold, "A nanomechanical mass sensor with yoctogram resolution," *Nature Nanotechnology*, vol. 7, p. 301–304, Apr. 2012.

[9] F. Khoshnoud and C. W. de Silva, "Recent advances in mems sensor technology-mechanical applications," *IEEE Instrumentation amp; Measurement Magazine*, vol. 15, p. 14–24, Apr. 2012.

[10] L. S. Collaboration, "Advanced ligo," *Classical and Quantum Gravity*, vol. 32, p. 074001, Mar. 2015.

[11] S. S. Verbridge, J. M. Parpia, R. B. Reichenbach, L. M. Bellan, and H. G. Craighead, "High quality factor resonance at room temperature with nanostrings under high tensile stress," *Journal of Applied Physics*, vol. 99, June 2006.

[12] P. Sadeghi, *Study of High-Q Nanomechanical Silicon Nitride Resonators*. PhD thesis, TU Wien, 2021. 10.34726/HSS.2021.50723.

[13] K. L. Ekinci, Y. T. Yang, and M. L. Roukes, "Ultimate limits to inertial mass sensing based upon nanoelectromechanical systems," *Journal of Applied Physics*, vol. 95, p. 2682–2689, Mar. 2004.

[14] Y. Tsaturyan, A. Barg, A. Simonsen, L. G. Villanueva, S. Schmid, A. Schliesser, and E. S. Polzik, "Demonstration of suppressed phonon tunneling losses in phononic bandgap shielded membrane resonators for high-q optomechanics," *Optics Express*, vol. 22, p. 6810, Mar. 2014.

[15] Y. Tsaturyan, A. Barg, E. S. Polzik, and A. Schliesser, "Ultracoherent nanomechanical resonators via soft clamping and dissipation dilution," *Nature Nanotechnology*, vol. 12, p. 776–783, June 2017. http://dx.doi.org/10.1038/nnano.2017.101.

[16] S. A. Fedorov, N. J. Engelsen, A. H. Ghadimi, M. J. Bereyhi, R. Schilling, D. J. Wilson, and T. J. Kippenberg, "Generalized dissipation dilution in strained mechanical resonators," *Physical Review B*, vol. 99, Feb. 2019. 10.1103/physrevb.99.054107.

[17] A. H. Ghadimi, S. A. Fedorov, N. J. Engelsen, M. J. Bereyhi, R. Schilling, D. J. Wilson, and T. J. Kippenberg, "Elastic strain engineering for ultralow mechanical dissipation," *Science*, vol. 360, p. 764–768, May 2018. 10.1126/science.aar6939.

[18] M. B. Kristensen, N. Kralj, E. C. Langman, and A. Schliesser, "Long-lived and efficient optomechanical memory for light," *Physical Review Letters*, vol. 132, Mar. 2024.

[19] G. Huang, A. Beccari, N. J. Engelsen, and T. J. Kippenberg, "Room-temperature quantum optomechanics using an ultralow noise cavity," *Nature*, vol. 626, p. 512–516, Feb. 2024.

[20] S. B. Cataño-Lopez, J. G. Santiago-Condori, K. Edamatsu, and N. Matsumoto, "High-q milligram-scale monolithic pendulum for quantum-limited gravity measurements," *Physical Review Letters*, vol. 124, June 2020.

[21] M. J. Bereyhi, A. Beccari, R. Groth, S. A. Fedorov, A. Arabmoheghi, T. J. Kippenberg, and N. J. Engelsen, "Hierarchical tensile structures with ultralow mechanical dissipation," *Nature Communications*, vol. 13, June 2022. 10.1038/s41467-022-30586-z.

[22] W. A. Phillips, "Two-level states in glasses," *Reports on Progress in Physics*, vol. 50, p. 1657–1708, Dec. 1987.

[23] J. Y. Lee, X. Lu, and Q. Lin, "High-q silicon carbide photonic-crystal cavities," *Applied Physics Letters*, vol. 106, Jan. 2015.

[24] E. Romero, V. M. Valenzuela, A. R. Kermany, L. Sementilli, F. Iacopi, and W. P. Bowen, "Engineering the dissipation of crystalline micromechanical resonators," *Physical Review Applied*, vol. 13, Apr. 2020.

[25] G. D. Cole, P.-L. Yu, C. Gärtner, K. Siquans, R. Moghadas Nia, J. Schmöle, J. Hoelscher-Obermaier, T. P. Purdy, W. Wieczorek, C. A. Regal, and M. Aspelmeyer, "Tensile-strained inxga1xp membranes for cavity optomechanics," *Applied Physics Letters*, vol. 104, May 2014.

[26] A. Beccari, D. A. Visani, S. A. Fedorov, M. J. Bereyhi, V. Boureau, N. J. Engelsen, and T. J. Kippenberg, "Strained crystalline nanomechanical resonators with quality factors above 10 billion," *Nature Physics*, vol. 18, p. 436–441, Feb. 2022.

[27] M. Naskar, P. K. Mishra, S. Ash, and A. K. Ganguli, "Superconductors with noncentrosymmetric crystal structures," *Bulletin of Materials Science*, vol. 44, Nov. 2021.

[28] P. J. Dobson, “Physical properties of crystals – their representation by tensors and matrices,” *Physics Bulletin*, vol. 36, p. 506–506, Dec. 1985.

[29] L. D. Landau, E. M. Lifshitz, J. B. Sykes, W. H. Reid, and E. H. Dill, “Theory of elasticity: Vol. 7 of course of theoretical physics,” *Physics Today*, vol. 13, p. 44–46, July 1960. 10.1063/1.3057037.

[30] S. Schmid, L. G. Villanueva, and M. L. Roukes, *Fundamentals of Nanomechanical Resonators*. Springer International Publishing, 2023. 10.1007/978-3-031-29628-4.

[31] A. N. Cleland and M. L. Roukes, “Noise processes in nanomechanical resonators,” *Journal of Applied Physics*, vol. 92, p. 2758–2769, Sept. 2002.

[32] M. H. J. de Jong, M. A. ten Wolde, A. Cupertino, S. Gröblacher, P. G. Steeneken, and R. A. Norte, “Mechanical dissipation by substrate–mode coupling in sin resonators,” *Applied Physics Letters*, vol. 121, July 2022. 10.1063/5.0092894.

[33] G. I. González and P. R. Saulson, “Brownian motion of a mass suspended by an anelastic wire,” *The Journal of the Acoustical Society of America*, vol. 96, p. 207–212, July 1994.

[34] M. Bao, H. Yang, H. Yin, and Y. Sun, “Energy transfer model for squeeze-film air damping in low vacuum,” *Journal of Micromechanics and Microengineering*, vol. 12, p. 341–346, Apr. 2002.

[35] I. Wilson-Rae, R. A. Barton, S. S. Verbridge, D. R. Southworth, B. Ilic, H. G. Craighead, and J. M. Parpia, “High-q nanomechanics via destructive interference of elastic waves,” *Physical Review Letters*, vol. 106, Jan. 2011.

[36] A. H. Ghadimi, “Ultra-coherent nano-mechanical resonators for quantum optomechanics at room temperature,” tech. rep., EPFL, 2018.

[37] M. J. Bereyhi, A. Arabmoheghi, A. Beccari, S. A. Fedorov, G. Huang, T. J. Kippenberg, and N. J. Engelsen, “Perimeter modes of nanomechanical resonators exhibit quality factors exceeding 10^9 at room temperature,” *Physical Review X*, vol. 12, May 2022.

[38] N. J. Engelsen, A. Beccari, and T. J. Kippenberg, “Ultrahigh-quality-factor micro- and nanomechanical resonators using dissipation dilution,” *Nature Nanotechnology*, vol. 19, p. 725–737, Mar. 2024. http://dx.doi.org/10.1038/s41565-023-01597-8.

[39] “Brillouin Zone construction — doitpoms.ac.uk.” https://www.doitpoms.ac.uk/tlplib/brillouin_zones/zone_construction.php. [Accessed 15-11-2024].

[40] “8.3: Brillouin Zone construction — eng.libretexts.org.” https://eng.libretexts.org/Bookshelves/Materials_Science/TLP_Library_I/08%3A_Brillouin_Zones/8.03%3A_Section_3-. [Accessed 15-11-2024].

[41] “memsconferences.org.” https://www.memsconferences.org/mems2021/images/current_support_files/spts/SPTS_Release_Etch_of_MEMS.pdf. [Accessed 22-11-2024].

[42] A. Hooper, J. Ehorn, M. Brand, and C. Bassett, “Review of wafer dicing techniques for via-middle process 3di/tsv ultrathin silicon device wafers,” in *2015 IEEE 65th Electronic Components and Technology Conference (ECTC)*, p. 1436–1446, IEEE, May 2015.

[43] S. K. Manjeshwar, *Free-space cavity optomechanical systems on a chip with III-V heterostructures*. PhD thesis, Chalmers Tekniska Hogskola (Sweden), 2023.

[44] S. Gröblacher, *Quantum Opto-Mechanics with Micromirrors: Combining Nano-Mechanics with Quantum Optics*. Springer Berlin Heidelberg, 2012.

[45] H. Bachor and T. C. Ralph, *A Guide to Experiments in Quantum Optics*. Wiley, July 2019.

[46] A. Dadgar, A. Krost, J. Christen, B. Bastek, F. Bertram, A. Krtschil, T. Hempel, J. Bläsing, U. Haboeck, and A. Hoffmann, “Movpe growth of high-quality aln,” *Journal of Crystal Growth*, vol. 297, p. 306–310, Dec. 2006. 10.1016/j.jcrysgro.2006.09.046.

[47] A. Ciers, A. Jung, J. Ciers, L. R. Nindito, H. Pfeifer, A. Dadgar, J. Bläsing, A. Strittmatter, and W. Wieczorek, “Thickness dependence of the mechanical properties of piezoelectric high-q_m nanomechanical resonators made from aluminium nitride,” 2024. 10.48550/ARXIV.2410.03944.

[48] *Proceedings of the Royal Society of London. Series A, Containing Papers of a Mathematical and Physical Character*, vol. 82, p. 172–175, May 1909. 10.1098/rspa.1909.0021.

[49] A. Ciers, A. Jung, J. Ciers, L. R. Nindito, H. Pfeifer, A. Dadgar, A. Strittmatter, and W. Wieczorek, “Nanomechanical crystalline aln resonators with high quality factors for quantum optoelectromechanics,” *Advanced Materials*, vol. 36, Sept. 2024. `10.1002/adma.202403155`.

[50] Y. Dai, S. Li, Q. Sun, Q. Peng, C. Gui, Y. Zhou, and S. Liu, “Properties of aln film grown on si (111),” *Journal of Crystal Growth*, vol. 435, p. 76–83, Feb. 2016. 10.1016/j.jcrysgro.2015.11.016.

[51] C. Brendel, V. Peano, O. Painter, and F. Marquardt, “Snowflake phononic topological insulator at the nanoscale,” *Physical Review B*, vol. 97, Jan. 2018. 10.1103/physrevb.97.020102.

[52] S. A. Saarinen, N. Kralj, E. C. Langman, Y. Tsaturyan, and A. Schliesser, “Laser cooling a membrane-in-the-middle system close to the quantum ground state from room temperature,” *Optica*, vol. 10, p. 364, Mar. 2023. 10.1364/optica.468590.

[53] “Periodic Condition — doc.comsol.com.” `https://doc.comsol.com/5.5/doc/com.comsol.help.sme/sme_ug_shell_plate.08.50.html`. [Accessed 21-11-2024].

A

Appendix A

A.1 Simulation parameter

thickness, h (nm)	90	145	195	295
σ_{residual} (GPa)	0.76	0.91	1.19	1.41
E (GPa)	313	308	329	272
Q_{int}	7.5×10^3	9.8×10^3	1.23×10^4	7.7×10^3
density, ρ (kg/m^3)	3255			
ν	0.287			

Table A.1: Material properties of AlN used as parameters in FEM simulations

DEPARTMENT OF MICROTECHNOLOGY AND NANOSCIENCE (MC2)
CHALMERS UNIVERSITY OF TECHNOLOGY
Gothenburg, Sweden
www.chalmers.se